The Numerical Renormalization Group and the Problem of Impurities in Metals

L. N. Oliveira

Instituto de Física e Química de São Carlos, Universidade de São Paulo

Caixa Postal 369, São Carlos, 13560-970, SP, Brasil

Received July 10, 1992

The numerical renormalization group approach to the computation of physical properties of impurities in metals is reviewed. The physical basis supporting the mathematical procediire is discussed and illustrated with a simple example: the numerical diagonalization of the analytically soluble $U = 0$ Anderson impurity Hamiltonian. Applications of the method aimed at determining (i) the fixed-point structure, (ii) the thermodynamical properties and (iii) the excitation properties of impurity Hamiltonians are surveyed. The method is compared with alternative approaches in the theory of localized excitations in metals.

I. Introduction

The interaction of a localized orbital with the conduction states in a metal raises intriguing questions. Studies of dilute magnetic alloys[1] first called attention to such interactions, but more recently it has become clear that they dominate the physics of chemisorption[2] and of a list of materials including valence-fluctuation[3] and heavy-fermion[4] compounds, and the superconducting oxides. It was early understood that, due to the interplay between correlation in the localized orbitals and their coupling to the conduction bands, measurements at different energy – or time – scales may yield qualitatively different physical interpretations. For example, at room temperature, the impurity contribution χ_{imp} to tlie magnetic susceptibility of a dilute CuFe alloy follows tlie Curie law characteristic of free-Fe d orbitals. In the Kelvin range, however, as the temperature T is lowered, the product $T\chi_{imp}$ approaches zero, which indicates that the magnetic moment has been quenched. Given the dilution of the impurities, the conflict between the two physical pictures cannot be attributed to phase transitions. When such discrepancies were first found, they seemed puzzling, and single-particle concepts appeared inadequate.

To the theorist, the coupling of the localized orbitals to the extended states posed yet another challenge. Traditicnal perturbation techniques proved inapplicable and special methods – in most cases adapted from particle physics – had to be developed to handle the strongly correlated electrons. That they were necessary, it was iealized in the early seventies[5], but the first quantitative acliievements were reported only in 1975.

In tliat year, severa1 authors used the numerical renormalization group approacli to calculate the temperature-dependent magnetic susceptibility for the Kondo[6] and Anderson[7] models for dilute magnetic alloys, as well as the low-temperature impurity contribution to the specific heat. The method identified the different high-temperature and low-temperature behaviours of the impurity magnetic moment with different *fixed* points of a renormalization-group transformation, thus solving the puzzle formed by the experimental data. Uniformly accurate over the parametrical spaces of the models, the procedure moreover provided a unifying view that gave proper perspective to previous theoretical results, such as the Schrieffer-Wolff canonical transformation of the Anderson Hamiltonian into the Kondo Hamiltonian [8].

In the last decade other approaches, analytical[9–11] or numerical[12] ones, have fully born out those results and extended them to more complex impurity Hamiltonians. Unfortunately, each of these latter methods has proved fruitful only in certain applications. The Bethe *ansatz*, for instance, has thoroughly surveyed the thermodynamical properties of a number of single-impurity Hamiltonians[9,13], but it has been much less succesful in dealing with dynamical properties and with impurity clusters. In view of such shortcomings, interest in the numerical renormalization group method has been continued, and the procedure has been extended to diagonalize two-impurity Hamiltonians[14–17] and to calculate excitation properties[17,18].

This review is dedicated to the numerical renormalization group. The problerns it has solved are examined, its limitations are indicated, and the perspectives for applications to more complex problerns discussed. Emphasis is placed on a particular aspect of the procedure: its ability to associate fixed points with a given Hamiltonian and thus to relate the physical properties of the model to special limits transparent to physical

interpretatiori.

Nine sections constitute this paper. Sections II and III discuss the physical foundation of the mathematical procedure. The general concept of scale invariance and its application to the metallic environment enclosing the impurities is examined. In Section IV, the procedure is outlined. The approximations – all of which are fully controllable – needed to make a model Hamiltonian numerically tractable are discussed. As an illustration, Section V diagonalizes the $U = 0$ Anderson Hamiltonian.

The next three sections review the three classes of results the numerical renormalization group method has produced. Section VI surveys computations of thermodynamical properties, Section VII discusses diagonalizations of model Hamiltonians, and Section VIII describes calculations of excitation properties. The final Section IX contains a brief evaluation of the approach and compares it with other methods.

II. Experimental Motivation

The first signals that the competition among energy (or time) scales can dominate the physics of impurities in metals came from the laboratory. In retrospect it is easy today to identify elements of scale-invariance breaking in a variety of experimental data, an example being the different magnetic moments of Fe in Cu at high and at low temperatures. In certain cases, however, the signals were so clear that the classification of the data into energy (or time) regimes was suggested at once. The most striking example is that of the valence-fluctuation compounds.

In the seventies, valence fluctuations were observed in a series of compounds of the lanthanides Ce, Sm, Eu, Tm, Yb, and of the actinide U. An often-quoted example is SmS, a semiconductor at amospheric pressure that turns metallic at hydrostatic pressures above 6 kbar [19]. In solids, the samarium ion is generally found in one of two valence states: Sm^{+2} ($4f^6$ configuration) or Sm^{+3} ($4f^5$ configuration). Hund's rules associate no magnetic moment with the forrner f-level configuration and approximately one Bohr magneton with the latter[22]. The ionic radius of Sm^{+2} is 1.14 A, significantly larger than the 0.96 A of Sm^{+3}. At atmospheric pressure, the valence of the samarium ion in SmS is +2. The transition to the metallic phase is accompanied by a reduction to an ionic radius intermediate between those of Sm^{+2} and Sm^{+3}. This reduction might be attributed to a valence change, the pressure having forced part of the ions into the higher-valence, smaller-volume state. This seems indeed confirmed by x-ray photoemission spectra[20], which can be divided into two spectra separated by several eV: one characteristic of the $4f^6$ configuration, the other characteristic of the $4f^5$ configuration.

Nonetheless, the isomer shift measured with Mossbauer spectroscopy shows that the ionic valence, uniform throughout the sample, lies between +2 and +3: instead of the two shifts characteristic of the $4f^6$ and of the $4f^5$ configurations, the Mossbauer spectrum for SmS shows a single shift between them[21]. Together, the two sets of data — photoemission and isomer shift — suggest that the valence of each Sm ion fluctuate between +2 and +3 at rste r_f of, say, $10^{12}\,s^{-1}$. The characteristic rate r_{exp} of the experimental technique (in spectroscopy, the characteristic rate is simply the typical width of a resonance divided by Planck's constant) must then be compared with r_f. If it is much larger than r_f, then each ion will be photographed in one of the two integer-valence states, part of them being pictured as Sm^{+2} and the rest as Sm^{+3}. This explains the photoemission spectra, for their characteristic rate is of the order of $10^{15}\,s^{-1}$, much larger than r_f. On the time scale of the fluctuations, photoemission is fast.

By contrast, Mossbauer spectroscopy involves slow measurements, with a characteristic rate of the order of $10^9\,s^{-1}$, significantly smaller than r_f. During the emission of the gamma-ray, the ion fluctuates several times between the two configurations, the result being an intermediate isomeric shift. One sees, therefore, that r_f divides the rate, or energy axis into two regimes: the fast and the slow domains.

That the same division characterizes the energetical dependence of other properties, it is shown by the susceptibility plots[23] for three Sm compounds in Figure 1. In SmTe and in SmS at $P = 0$, the samarium ion is divalent; in $SmPd_3$, it is trivalent. The susceptibility plot for the latter shows a Curie behavior, a temperature dependence that is expected, given the magnetic moment of the $4f^5$ configuration. For the former two, the weakly temperature-dependent susceptibility is due to low-lying excited states[22].

Compare those three curves with the plot for SmS under pressure. At each temperature T, the exchange of temperature with the thermal reservoir occurs at the rate $r_T = k_B T/\hbar$, which is then the characteristic frequency of a thermodynamical measurement. At high temperatures ($T \gg 50$ K), tlie thermal rate r_T is much larger than r_f; like the photoemission spectrum, the susceptibility is a statistical average between χ for the $4f^6$ and the $4f^5$ configurations and hence must lie between the two. The SmS ($P > 7.5$ kbar) plot in Figure 1 confirrns this reasoning.

At low temperatures ($T \ll 50$ K), on the other hand, r_T is smaller than r_f. Now, as in the Mossbauer measurement, the Sm ion has time to fluctuate between the two valences during a measurement; it is therefore found in a quantum state that is a linear combination of the $4f^6$ and $4f^5$ configurations. The measured susceptibility is a quantum average – i. e., an average including interference – between the two valences and needs not be intermediate between the Sm^{+2} and Sm^{+3} susceptibilities. Figure 1 bears this out, too.

As this example shows, the concept of competi-

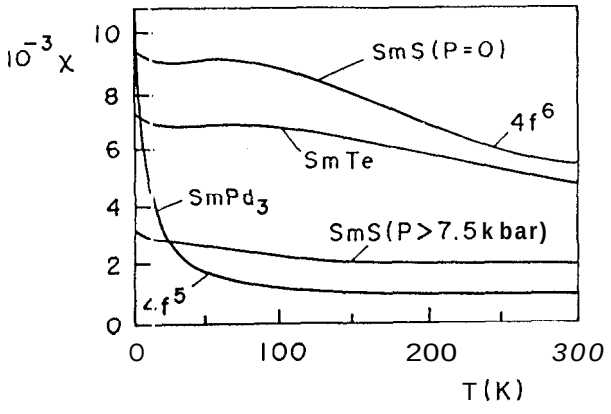

Figure 1.: Susceptibility (in esu/mole) as a function of temperature for three Sm compounds, adapted from Ref. 23. In SmTe and SmS at zero pressure, the Sm ion is divalent ($4f^6$ configuration). In $SmPd_3$, it is trivalent ($4f^5$) and its magnetic moment accounts for the Curie behavior. At pressures above 6 kbar, the Sm ion in SmS is in an fluctuating-valence state. As discussed in the text, at high temperatures ($T > 100$ K), the susceptibility is a statistical average between those for the $4f^6$ and the $4f^5$ configurations and must lie between them. At low temperatures ($T < 20$ K), however, the susceptibility measurement probes a linear combination between the $4f^6$ and $4f^5$ configurations.

tion between energy scales is germane to the valence-fluctuation prcblem and more extensively to the problem of strongly correlated electrons in metals. It should not come as a surprise, therefore, that a numerical method exploring scale invariance should be accurate or that it should provide physical insight even into models whose physical properties technical difficulties prevent it from computing.

Valence fluctuations, for example, are described by the Anderson impurity model[24], whose Hamiltonian was diagonalized and whose thermodynamical properties were calculated by the numerical renormalization group method sver a decade ago[7,25]. At the time, the numerical protedure that computes excitation properties still undrveloped, and the photoemission spectrum could not be calculated. Nevertheless, on the basis of the insight provided by the numerical diagonalization of the model Hamiltonian combined with a few exact results and sum rules, Wilkins[26] provided a semi-quantitative description of the spectrum, later perfected by $1/N$-expansion[27] and renormalization-group[18] computations.

Another example is the heavy-fermion problem. Certain compounds of lanthanides (e. g., $CeCu_2Si_2$, $CeAl_3$, YbCuAl) or actinides (e. g., UBe_{13}, UPt_3, $NpBe_{13}$) show anomalously high linear specific-lieat coefficients γ at moderately low temperatures (typically, $T > 1$ K)[28]; the highly-massive low-energy quasiparticles in such systems have been named heavy fermions. In disparity with normal metals, for which γ is of the order of $1 mJ/mol K^2$ [22], the coefficient for a heavy-fermion compound is larger than $100 mJ/mol K^2$: for $CeCu_2Si_2$, the first-discovered heavy-fermion system, $\gamma = 1000 mJ/mol K^2$. Such enormous y's, as shown in Section VI, are expected of strongly correlated impurities in metals, and indeed the physical properties of heavy fermions measured at moderately low energies are well described by the Anderson single-impurity Hamiltonian, the 4f orbitals of the lanthanide or the 5f orbitals of the actinide represented by impurity levels.

Nonetheless. the rare-earth ions are not impurities[29]. They are part of the lattice, and this has clear experimental consequences: at sufficiently low temperatures (typically, $T < 1$ K) the heavy-fermion systerns deviate from the impurity behavior, becoming superconductive or antiferromagnetic. The different behaviors at moderately low and at very low temperatures define two temperature regimes and point to a characteristic energy separating them, of the order of $k_B T^*$, wliere T^*, the coherence temperature, is of the order of $1 K$. Clearly, $k_B T^*$ defines an effective coupling between f levels on neighboring sites. For $T \gg T^*$, that coupling is negligible, and the f orbitals behave as independent impurities. For $T \ll T'$, on the other hand, the intersite coupling dominates the physics. In Section VIII, a simple model will provide a concrete illustration of these concepts. Although too crude to describe even qualitatively the physical properties of the heavy fermions, that model helps one to understand the success of the impurity Hamiltonians[30].

These examples serve as motivation for a scaling analysis, but fail to identify the characteristics of a metal that make one such approach productive. The following section searches for those characteristics and show that the energy scale invariance of the conduction band accounts for the achievements of the numerical renormalization group method.

III. Theoretical Motivation

A. Scale Invariance

The theory of the renormalization group explores the scaling properties of physical systems. Many systems are invariant under scale transformations. In condensed matter physics, the most widely known example is the ferromagnet at criticality. At any ternperature T, distances in a ferromagnet can be compared with two characteristic lengths: the lattice parameter a and the correlation length ξ. An experimental technique probing a sample at the length scale L will in general yield results dependent upon the ratios L/a and L/ξ. At the critica1 temperature T_c, the correlation length diverges, and the latter ratio vanishes. If in addition L is

large on the atomic scale, then L/a is essentially infinite, and two measurements taken at the length scales L and $L' = \Lambda L$ (wliere A is any number larger than unity) should yield qualitatively the same results. By contrast, at temperatures different from T_c the correlation length is finite, so that the outcomes of two measurements at the scales $L < \xi$ and $L' > \xi$ will in general show qualitative differences.

In renormalization-group analyses of a model for the ferromagnet, the scaling $L \rightarrow \Lambda L$ is constructed mathematically, which defines a *renormalization-group transformation*. A temperature T is then considered, and the transformation is applied repeatedly to the model Hamiltonian H. If one starts out with $L = L_0 = a$, then after n transformations the system is being probed at the scale $L, = (\Lambda)^n a$.

As n increases, the Boltzmann weight of any given eigenvalue of the Hamiltonian will in general change. A schematical plot of the n dependence of one such weight for a temperature somewhat below the critical temperature appears in Figure 2. The plot divides the horizontal axis into four domains with boundaries at n = N_1, N_2, and N_3. For small n tlie weight shows a weak n dependence, which dies out as the index grows. As n becomes larger than N_1, the Boltzmann weight remains nearly invariant for several transformations. As it approaches N_2, however, it begins to grow out of that plateau; between n = N_2 and n = N_3, it rises rapidly, to saturate at a higher level.

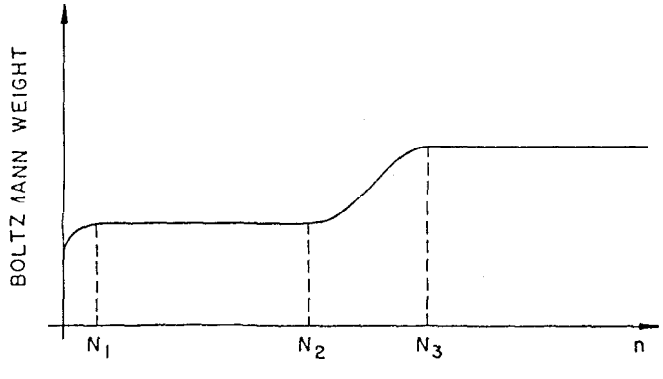

Figure 2.: Dependence of Boltzmann weight W = $\exp -E/k_B T$ on the renormalization-group transformation index n (schematical). E is an eigenvalue of the model Hamiltonian, and n is the number of times the model has been subject to the scaling transformation $L \rightarrow \Lambda L$. As discussed in the text, the two plateaus, between n = N_1 and n = N_2, and for n > N_3, respectively, are associated with fixed points. The rapid change between N_2 and N_3 is a crossover.

Scaling concepts explain this evolution. In the first transformations, the length scale L, is comparable to the lattice parameter a. The Boltzmann factor, as well as the physical properties of tlie model, are therefore expected to depend on the ratio L_n/a. which explains the initial n dependence in Figure 2. With growing L_n, that ratio becomes larger and larger; as it approaches infinity, it influences less and less the Boltzmann weight. The lattice parameter is an *irrelevant length*, a feature of the model that becomes immaterial for sufficiently large n.

For n = N_1, the lattice parameter negligible in comparison with L_n, the plot in Figure 2 reaches the first plateau. Here, albeit much larger than a, the length scale L, is much smaller than the correlation length ξ. If ξ were infinite, there would be no length scale, and the Boltzmann weight, invariant under scaling, would be a *fixed point* of the renormalization-group transformation. For $N_1 <$ n $< N_2$, the weight is close to that fixed point since L_n/ξ is very small.

As n increases, however, L_n/ξ grows. Eventually, for n $\approx N_2$, the ratio becomes significant and affects the Boltzmann weight. In the first plateau (close to the fixed point) the coherence length is *relevant*: its importance grows exponentially with n, and it drives the model away from the fixed point.

In the *crossover* region ($N_2 <$ n $< N_3$), the Boltzmann weight changes rapidly as the ratio L_n/ξ grows from much smaller than unity to much larger than unity. After that, less and less significant in comparison with L_n, the correlation length is irrelevant, and the weight approaches a second fixed point.

B. Conduction States

The physical properties of a metal contaning impurities are markedly different from those of a ferromagnet. In special, the impurities can cause no phase transitions. Nonetheless, the two systems have similar scaling properties. Figure 2 describes metallic impurities as well as it describes the ferromagnet.

For the metal, the scaling involves energies, instead of lengths. The only characteristic energy in a metallic conduction band is the Fermi energy ε_F. The pure metal is therefore akin to the ferromagnet at the critical temperature, which has a single characteristic length scale—the lattice parameter. If the pure metal is probed at the energy $\epsilon \ll \varepsilon_F$, then its properties are qualitatively independent of ϵ.

Impurities, which generally have characteristic energies, break this scale invariance. A metal with impurities is analogous to a ferromagnet somewhat below (or above) the critical temperature. In Section IV, a renormalization-group transformation will be introduced that amounts to the scaling $\epsilon \rightarrow \epsilon\Lambda$, where again A is any number larger than unity. Given a model for a metal with impurities, one starts out at the energy $\epsilon_0 = \varepsilon_F$ and scales down to the energy $\epsilon_n = \varepsilon_F/\Lambda^n$. At a given temperature T, the Boltzmann weight associated with any eigenvalue of the model Hamiltonian changes with n according to the pattern in Figure 2.

As in Section IIIA, scaling concepts help us understand that behaviour. Suppose that a thermodynamical property is measured at a variety of temperatures, ranging from very high, comparable with the Fermi energy, to very low. At each temperature, the system is probed at the energy scale k_BT, where k_B is the Boltzmann constant. Hence the sequence of measurements then can be paced in correspondence with the sequence of energies ϵ_n. For small n, the conduction band is probed at large-energy scales, energies comparable to the Fermi energy. The Boltzmann weight associated with the temperature T such that $k_BT = \epsilon_n$ depends on the ratio $k_BT/\varepsilon_F = \epsilon_n/\varepsilon_F$ and therefore changes with n. As the index grows, however, ϵ_n diminishes, and the ratio ϵ_n/ε_F becomes negligible. Consequently, as n approaches N_1, the Boltzmann weight tends to stabilize. The Fermi energy is irrelevant.

For a pure metal, the first plateau in Figure 2 would be infinite. In the absence of characteristic energies, the Boltzmann weight remains invariant under the renormalization-group transformation, i. e., it is a fixed point of the transformation. The end of the plateau in the illustration is due to an impurity with a small energy splitting Δ. For small n, the energy scale ϵ_n is much larger than Δ, so that the splitting is unimportant. After successive renormalization-group transformations, however, ϵ_n is so reduced that the ratio Δ/ϵ_n becomes significant. This indicates that, in the first plateau, Δ is a relevant energy.

Subsequent increases in n drive the Boltzmann factor away from the fixed point, as the crossover in Figure 2 indicates. After a few more transformations, the weight is again independent of ϵ_n, for the ratio Δ/ϵ_n is essentially infinite. The weight reaches the second plateau in the figure; here, Δ is irrelevant.

As this discussion indicates, the renormalization-group theory of impurities in metals explores energy-scale invariance. Since experiments have characteristic energies, the connection between flow diagrams for such systems and experimental results is particularly tight. In special, plots analogous to the one in Figure 2 assist the interpretation of laboratory data, and the fixed-point structure of a model Hamiltonian explains qualitatively its physical properties. This aspect of the renormalization-group approach will be further discussed in Sections VI-VIII; before that, however, the mathematical foundations of the procedure must be introduced.

IV. Mathematical Procedure

A. Logarithmic Discretization

Although ultimately relying on a numerical diagonalization of the model Hamiltonian, the renormalization-group method is by no means one of brute force. Prior to the diagonalization, the conduction-band Hamiltonian H_c is projected on a special basis, defined to preserve the energy-scale invariance of the conduction band. This paves the way to the definition of a renormalization-group transformation. Moreover, the chosen basis ensures that the projection does not affect the coupling of the conduction band to the impurity; with this, uniform accuracy over the parametrical space of the Hamiltonian is guaranteed. Finally, although the basis is incomplete with respect to the conduction states, so that the projected Hamiltonian is an approximation to H_c, a parameter Λ gives full control over that approximation. The resulting numerical procedure is essentially exact: typically, maximum deviations of a few percent are obtained when a thermodynamical (excitation) property is computed at any given temperature (frequency).

The impurity Hamiltonians to which the procedure applies have the form

$$H = H_{imp} + H_c + H_{imp-c}, \tag{1}$$

where H_{imp}, H_c, and H_{imp-c} are the impurity Hamiltonian, the conduction-band Hamiltonian, and the impurity-to-band coupling, respectively. An example is the spin-degenerate Anderson Hamiltonian, for which

$$H_{imp} = \sum_{\mu} \epsilon_f c^{\dagger}_{f\mu} c_{f\mu} + U n_{f\uparrow} n_{f\downarrow}, \tag{2}$$

where ϵ_f is the impurity-orbital energy, U is the Coulomb repulsion at the impurity site, and $n_{f\mu} = c^{\dagger}_{f\mu} c_{f\mu}$ denotes the μ-spin impurity occupation. The coupling to the conduction band is

$$H_{imp-c} = \sqrt{2} V \sum_{\mu} f^{\dagger}_{0\mu} c_{f\mu} + \text{H. c.}, \tag{3}$$

where the normalized Fermi operator $f_{0\mu}$ is a shorthand for a sum over the conduction states:

$$f_{0\mu} = 1/\sqrt{2} \sum_{k} c_{k\mu}. \tag{4}$$

The conduction band Hamiltonian describes noninteracting spin-degenerate electrons:

$$H_c = \sum_{k\mu} \epsilon_k c^{\dagger}_{k\mu} c_{k\mu}. \tag{5}$$

The energies ϵ_k are measured from the Fermi level, and the momenta k from the Fermi momentum k_F. Since one is interested in small energies, a half-filled band with the linear dispersion relation

$$\epsilon_k = k/k_F D \qquad (-D < \epsilon_k < D) \tag{6}$$

is traditionally considered.

The continuum of the conduction levels being unwieldy for numerical treatment, the conduction band must be discretized. The logarithmic discretization in Figure 3 preserves scale invariance. Its definition involves two dimensionless parameters, Λ and z. The

former must be larger than unity, but is otherwise arbitrary. The latter can be any number between 0 and 1. The original definition[6,7] of the renormalization-group procedure makes no reference to z (to recover that definition, one must set $z = 1$ in Figure 3). As it will be shown below, however, in calculations of excitation properties the recently introduced parameter[18,31] is indispensable. A discussion of the generalized (z-dependent) procedure seems therefore appropriate.

The definition of the discretized basis follows the prescription spelled out in Ref.6. For each of the conduction-energy intervals $\Lambda^{-m-z} \geq \pm\epsilon_k/D > \Lambda^{-m-1-z}$ ($m = 0,\ldots,\infty$) in Figure 3, a single normalized Fermi operator $a_{m\pm}^{\dagger}$ is defined, equal to the most localized state around the impurity site that can be constructed out of the c_k's:

$$a_{m\pm} = \pm(1-\Lambda^{-1})^{-1/2} \int_{\pm D\Lambda^{-m-1-z}}^{\pm D\Lambda^{-m-z}} c_k \, dk. \qquad (7)$$

For the two intervals closest to the band edges, one defines

$$a_{\pm} = \pm(1-\Lambda^{-z})^{-1/2} \int_{+D\Lambda^{-z}}^{\pm D} c_k \, dk. \qquad (8)$$

The basis of the $a_{\pm}$ is evidently incomplete with respect to the c_k. In the following section, the model Hamiltonian will be projected on this incomplete basis. Justification for this approximation is provided by a two-step argument due to Wilson[6] and Krishnamurthy et al.[7]. These authors first observed that, for $\Lambda \rightarrow 1$, the conduction-band Hamiltonian projected on the basis of the $a_{\pm}$ is equivalent to the Hamiltonian (5). Next, they presented three evidences that thermodynamical properties calculated with $\Lambda > 1$ converge very rapidly to the continuum limit: (i) near fixed points, where physical properties of model Hamiltonians can be computed analytically, the deviation of a thermodynamical average computed at given temperature with given Λ from its continuum-lirnit value is proportional to $\exp(-\pi^2/\ln\Lambda)$; (ii) for special parametric choices (see Section V), the Anderson Hamiltonian can be diagonalized analytically; when its thermodynamical properties are calculated for given Λ, they again deviate from the continuum limit by amounts proportional to $\exp(-\pi^2/\ln\Lambda)$; (iii) for parametrical choices impeding analytical diagonalization, any thermodynamical average (A) calculated numerically at a given temperature is found to have the following Λ dependence:

$$\langle A \rangle = A_0 + ce^{-\pi^2/\ln\Lambda}, \qquad (9)$$

where A_0 is independent of Λ, and c depends only weakly on the discretization parameter. Since the publication of Ref. 6, a substantial mass of numerical and analytical results has accrued on these findings, and in Ref. 31 it was found indications that the convergence of excitation properties to the continuum limit is even faster. Such findings show that calculations carried out with, e. g., $\Lambda = 3$ are representative of the continuum limit. To check this conclusion by studying the Λ dependente of computed physical properties is a routine procedure in renormalization-group calculations. With this indispensable precaution, the discretization is justified.

B. Basis Transformation

The operators $a_{\pm}$ and $a_{m\pm}$ ($m = 0,\ldots,\infty$) form a basis onto which the conduction-band Hamiltonian can be projected. The projected Hamiltonian is an infinite series, more convenient than the continuum in Eq. (5), but still unfit for numerical processing. The series has to be truncated.

Before that, however, attention must given to the coupling to the impurity. As (3) indicates, H_{imp-c} involves the Wannier state $f_{0\mu}$. In order to preserve the integrity of the coupling Hamiltonian, the truncation must not affect that ferrnionic operator. Accordingly, prior to being truncated, the discretized Hamiltonian is subjected to a Lanczos transformation[32]: a second orthonormal basis of fermionic operators $f_{n\mu}$ ($n = 0,1,\ldots$) is defined, each a linear combination of the $a_{\pm}$ and $a_{m\pm}$ ($m=0,1,\ldots$). Here, $f_{0\mu}$ is the operator in Eq. (4), and the remaining f_n are defined[32] to make the conduction-band Hamiltonian H, tridiagonal:

$$H_c = \sum_{\mu,n=0}^{\infty} \epsilon_n^z (f_{n,\mu}^{\dagger} f_{n+1,\mu} + \text{H. c.}). \qquad (10)$$

The coefficients ϵ_n^z are determined by solving recursively the following equation[31]:

$$\prod_{n=0}^{N} (\epsilon_n^z)^2 = F_N(z,\Lambda) - [(\mathcal{H}_{N+1})^{2N+2}]_{11}, \qquad (11)$$

where the term within the square brackets on the right-hand side is the $2N+2$th power of the tridiagonal matrix

$$[\mathcal{H}_{N+1}]_{ij} = \epsilon_{i-1}^z \delta_{i,j-1} + \epsilon_{j-1}^z \delta_{j,i-1}. \quad (i,j = 1,2,\cdots,N+1). \qquad (12)$$

The first term on the right-hand-side of Eq. (11) is the function

$$F_N(z,\Lambda) = (1-\Lambda^{-1}) \sum_{m=0}^{\infty} \Lambda^{-z-m} \times \left[D\frac{(1+\Lambda^{-1})}{2}\Lambda^{-m-z-1}\right]^{2N+2} + (1-\Lambda^{-z}) \times \left[D\frac{(1+\Lambda^{-z})}{2}\right]^{2N+2} \qquad (13)$$

For $N = 0$, the matrix $\mathcal{H}_1$ contains a single element, $[\mathcal{H}_1]_{11} = 0$, so that the last term on the right-hand

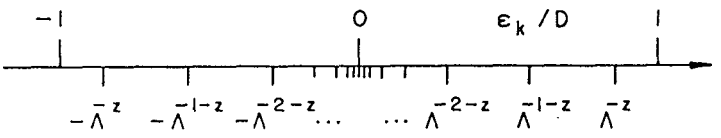

Figure **3.:** Logarithmic discretization of the conduction band. **A** must be larger than unity and r must lie between 0 and 1; otherwise, the two parameters are arbitrary.

side of Eq. (11) vanishes. That equation can therefore be solved for ϵ_0^z. For N > 0, once the $\epsilon_0^z, \ldots, \epsilon_{N-1}^z$ have been calculated, Eq. (12) determines the matrix $\mathcal{H}_{N+1}$, and the right-hand side of Eq. (5) can again be computed. On the left-hand side, the only unknown is ϵ_N^z, which can therefore be computed. For large N, it can be shown[31] that ϵ_N^z decreases exponentially with N:

$$\epsilon_N^z \approx (1+\Lambda^{-1}/2)D\Lambda^{1-z-N/2} \qquad (N \gg 1). \qquad (14)$$

This conipletes the basis transformation. Eq. (4) is substituted for H, in Eq. (1). The result is the model Hamiltonian projected on the basis of the operators $f_{n\mu}$ (n = 0, 1, ...) and $c_{f\mu}$:

$$\begin{aligned} H &= \sum_{\mu,n=0}^{\infty} \epsilon_n^z (f_{n\mu}^\dagger f_{n+1\mu} + \text{H. c.}) \\ &\quad + \sqrt{2}V(f_{0\mu}^\dagger c_{f\mu} + \text{H. c.}) \\ &\quad + \sum_{\mu} \epsilon_f c_{f\mu}^\dagger c_{f\mu} + U n_{f\uparrow} n_{f\downarrow}. \end{aligned} \qquad (15)$$

C. Truncaticn and Diagonalization

Equation (15) is in appropriate form for truncation. According tc Eq. (14), ϵ_n^z decays exponentially with n. If one is interested, for instance, in a thermodynamical property at the temperature T, then energies much smaller than $k_B T$ are unimportant. It follows that the infinite series on the right-hand side of Eq. (15) can be truncated at n = N − 1, where N is an integer such that $\epsilon_N^z \ll k_B T$.

To be more specific, one reverses the relation between N and T. For given N, one defines the energy

$$D_N = (1+\Lambda^{-1}/2)D\Lambda^{-[z+(N-3)/2]}, \qquad (16)$$

which is approximately equal to ϵ_{N-1}^z (the symbol D_N is a reminder that, for N = 1, this energy is comparable to the half bandwidth D), and chooses the temperature T so that

$$k_B T = D_N/\alpha, \qquad (17)$$

where o is a small constant, o = 0.1 for iiistance. This guarantees ϵ_N^z to be much smaller than $k_B T$.

To a good approximation, then, the Hamiltonian in Eq. (15) can be written

$$\begin{aligned} H &= \sum_{n=0}^{N-1} \epsilon_n^z (f_n^\dagger f_{n+1} + \text{H. c.}) \\ &\quad + \sqrt{2}V(f_{0\mu}^\dagger c_{f\mu} + \text{H. c.}) \\ &\quad + \sum_{\mu} \epsilon_f c_{f\mu}^\dagger c_{f\mu} + U n_{f\uparrow} n_{f\downarrow}. \end{aligned} \qquad (18)$$

One is now in position to define a renormalization-group transformation. To this end, the truncated Harniltonian is divided by the factor D_N, which defines the scaled, dimensionless Hamiltonian

$$\begin{aligned} H_N &= \Bigg[\sum_{n=0}^{N-1} \epsilon_n^z (f_n^\dagger f_{n+1} + \text{H. c.}) \\ &\quad + \sqrt{2}V(f_{0\mu}^\dagger c_{f\mu} + \text{H. c.}) \\ &\quad + \sum_{\mu} \epsilon_f c_{f\mu}^\dagger c_{f\mu} + U n_{f\uparrow} n_{f\downarrow} \Bigg] / D_N, \end{aligned} \qquad (19)$$

in which the smallest Lanczos coefficient, ϵ_{N-1}^z/D_N, is approximately equal to 1. As N grows, new conduction terms are added to the truncated Hamiltonian, but the scaling ensures that each new term is of the order of unity. Thus, if there were no impurity, the smallest energies in the scaled Hamiltonian would be independent of N, i. e., scale invariant. Since the coupling to the impiirity [the second term on the right-hand side of Eq. (19)] and the irnpurity terrns (the third and fourth terms) grow with N, the impurity can break that invariance, as anticipated in Section III.

Notice that, in view of Eq. (17), the scaled Hamiltonian is proportional to the exponent $H/k_B T$ of the Boltzmann factor:

$$e^{-H/k_B T} \equiv e^{-\alpha H_N}, \qquad (20)$$

a feature that simplifies the computation of thermodynamical properties.

Mathematically, the renormalization-group transformation $\mathcal{T}$ is defined by the changes H_N undergoes as N increases:

$$\mathcal{T}[H_N] = H_{N+1} = \sqrt{\Lambda} H_N + \epsilon_N^z (f_N^\dagger f_{N+1} + \text{H. c.})/D_N. \qquad (21)$$

The form (19) is also appropriate for numerical diagonalization. This iterative procedure starts out with $N = 0$, so that the conduction-band Hamiltonian [the first term on the right-hand side of Eq. (18)] vanishes. The remaining terms can be diagonalized analytically (Hamiltonians more complex than that of the Anderson model may call for numerical computation even at this early stage; nonetheless, since the impurity Hamiltonian comprises only a few terms, its diagonalization is always a simple numerical exercise). From each eigenvalue, the smallest one is subtracted, so that all energies are measured with respect to the ground state.

The $H_{N=0}$ Hamiltonian is a 16×16 matrix, since sixteen many-body basis states can be constructed out of the operators $f_{0\mu}$ and $c_{f\mu}$. To proceed to $N = 1$, one has to add $f_{1\mu}$ to that list. In other words, out of each eigenvector $|\phi\rangle$ of H_0, four basis states have to be constructed: $|\phi\rangle$, $f_{1\uparrow}^\dagger|\phi\rangle$, $f_{1\downarrow}^\dagger|\phi\rangle$, and $f_{1\uparrow}^\dagger f_{1\downarrow}^\dagger|\phi\rangle$. In the basis of these states, the truncated Hamiltonian is a 64×64 matrix that can be diagonalized numerically. Again, from each resulting eigenvalue the smallest one is subtracted. Out of each eigenvector $|\varphi\rangle$, four new basis states ($|\varphi\rangle$, $f_{2\uparrow}^\dagger|\varphi\rangle$, $f_{2\downarrow}^\dagger|\varphi\rangle$, and $f_{2\uparrow}^\dagger f_{2\downarrow}^\dagger|\varphi\rangle$) are constructed. The entire cycle is repeated for $N = 2$, and then for $N = 3$, and so forth.

Clearly, the number of basis states increases in proportion to 4^N. If unchecked, such a growth would rapidly exhaust even the richest computational resources. Practical considerations are therefore necessary, to restrict the number of states taken into account in each iteration.

As an illustration, consider the computation of a thermodynamical property, at the temperature T. According to Eq. (17), the smallest energy resulting from the diagonalization of the model Hamiltonian will be of the order of $\epsilon_{min} \approx \alpha k_B T$, to which corresponds a Boltzmann weight $\exp(-\epsilon_{min}/k_B T) = \exp(-\alpha)$, approximately equal to unity (since a is small). Larger energies will be associated with smaller Boltzmann factors. If one chooses to neglect weights below a minimum w_{min}, then energies above a maximum ϵ_{max} such that $\exp(-\epsilon_{max}/k_B T) = w_{min}$ can be disregarded.

The numerical diagonalization determines the eigenvalues of the scaled Hamiltonian H_N. Each of these is equal to an energy scaled by $\Lambda^{z+(N-3)/2}$. In particular, the smallest scaled eigenvalue, proportional to ϵ_{min}, is of the order of unity, while the largest eigenvalue that must be taken into account is

$$E_{max} \approx \epsilon_{max} \Lambda^{z+(N-3)/2} \approx \epsilon_{max}/\alpha k_B T. \qquad (22)$$

In practice, therefore, a band of eigenvalues, bounded below by unity and above by E_{max}, is considered after each numerical diagonalization. If H_N were a fixed point of the renormalization-group transformation, the number of eigenstates between 1 and E_{max} would be rigorously independent of N. Since H_N is generally not a fixed point, that number may vary with N; the variations are nevertheless small, so that matrices of essentially the same dimensions have to be diagonalized in each iterations. The computational cost grows linearly—not exponentially—with N.

To further reduce the computational effort, prior to each diagonalization the basis states are combined into eigenstates of the electronic charge, and spin (and axial charge[15,16], if the model is particle-hole symmetric)—which are conserved; this reduces substantially the dimensions of the matrices to be diagonalized. For the spin-degenerate Anderson model, these rneasures reduce the CPU time required for a full diagonalization of the model Hamiltonian on a VAX-6400 to a few minutes. Models with larger numbers of degrees of freedom can be considerably—and often prohibitively—more demanding.

This concludes our discussion of the general aspects of the mathematical procedure. As an illustration, Section V discusses the diagonalization of the Anderson Harniltonian for $\epsilon_f = U = 0$. More interesting results are discussed in Sections VI-VIII.

V. The $\epsilon_f = U = 0$ Anderson Hamiltonian

The only quartic term in the Anderson Hamiltonian is proportional to the Coulomb repulsion U. For $U = 0$, the quadratic Hamiltonian can be diagonalized analytically[1]. One then finds that the coupling V to the conduction band broadens the impurity level to a width

$$\Gamma = \pi V^2/D. \qquad (23)$$

With $\epsilon_f = 0$, this width is the only characteristic energy associated with the impurity.

The coupling to the impurity phase shifts the conduction levels. Those removed in energy from ϵ_f are not affected, but those in the region $|\epsilon - \epsilon_f| \lesssim \Gamma$ are strongly shifted. In particular, for $|\epsilon - \epsilon_f| \ll \Gamma$, the phase shift is $\pi/2$.

Consider now the renormalization-group treatment of the model Hamiltonian. For vanishing orbital energy and Coulomb repulsion, the scaled Anderson Hamiltonian in Eq. (19) becomes

$$H_N = \left[\sum_{n=0}^{N-1} \epsilon_n^z (f_n^\dagger f_{n+1} + \text{H c.}) + \sqrt{2}V(f_{0\mu}^\dagger c_{f\mu} + hc)\right]/D_N. \qquad (24)$$

The $\uparrow$ and $\downarrow$ spin indices, labeling states that are decoupled from each other and degenerate, can be disregarded.

The quadratic form (24) can be diagonalized by a straightforward procedure, one that is simpler than the iterative method in Section IV C. We rewrite its right-hand side as a matrix:

$$H_N = v^\dagger \mathcal{H} v, \qquad (25)$$

where the vector v is defined by the equality

$$v^{\dagger} = (c_f^{\dagger}, f_0^{\dagger}, f_1^{\dagger}, \ldots, f_N^{\dagger}), \tag{26}$$

and H is a (IJ + 2) × (N + 2) codiagonal matrix whose elements are

$$\mathcal{H}_{1,2} = \mathcal{H}_{2,1} = \sqrt{2}V/D_N, \tag{27}$$

and

$$\mathcal{H}_{n+1,n+2} = \mathcal{H}_{n+2,n+1} = \epsilon_{n-1}/D_N \quad (n = 1, 2, \ldots, N). \tag{28}$$

When $\mathcal{H}_\Lambda$ is diagonalized numerically, N + 2 eigenvalues are found. Since H_N in Eq. **(24)** is particle-hole symmetric, i. e., it remains invariant under the transformation $f_n \rightarrow (-1)^{n+1} f_n^{\dagger}$ (n = 0, 1, ...), for each eigenvalue η there must be a symmetric eigenvalue $-\eta$. For even N, then, the N + 2 eigenvalues form two symmetrical groups, half of them being positive and half negative. For odd N, one must be zero, and the remaining ones again form two symmetrical sets.

Figure 4 shows an example. For clarity, only the odd-N pattern is shown. The pattern for even N is analogous (although different). The eigenvalues in the figure were calculated for $\Gamma = 10^{-4}D$. The non-zero eigenvalues are denoted $\pm\eta_j^N$, with j = 1, 2,..., (N + 1)/2, in order of increasing absolute value.

As N grows, new eigenvalues appear, but the ones closest to zero show a clear pattern. After the first few N, those eigenvalues stabilize and remain essentially fixed until N = 20. Rapid changes follow, but for N > 25, the eigenvalues again become independent of N.

This behaviour reproduces the main features of Figure 2. In the first plateau (N < 20), the scaled Hamiltonian is close to a fixed point, but a relevant energy drives it away from it, towards a second fixed point, to wliich H_N comes close in the second plateau.

Physically, the two fixed points reflect the energy scaling invariance of the conduction band, broken only by the broadening Γ, of the impurity energy by the conduction state:;. For large energies ϵ (i. e., for small N), that width is negligible, so that the coupling to the impurity can be disregarded. This approximation reduces the model Hamiltonian to the conduction Hamiltonian, which is a fixed point.

This interpretation is confirmed by the inset. Here, the energies ϵ_j, associated with the eigenvalues η_j^N by the scaling

$$\epsilon_j = D_N \eta_J^N, \tag{29}$$

are plotted as functions of N. While the main plot shows the η_j^N closest to zero, the inset shows all energies, only the ones that are largest in absolute value being well resolved. Inspection of the plot shows that it reproduces quantitatively the logarithmic discretization of the conduction band in Figure **3.** Clearly, the energies farthest away from zero are the energy levels

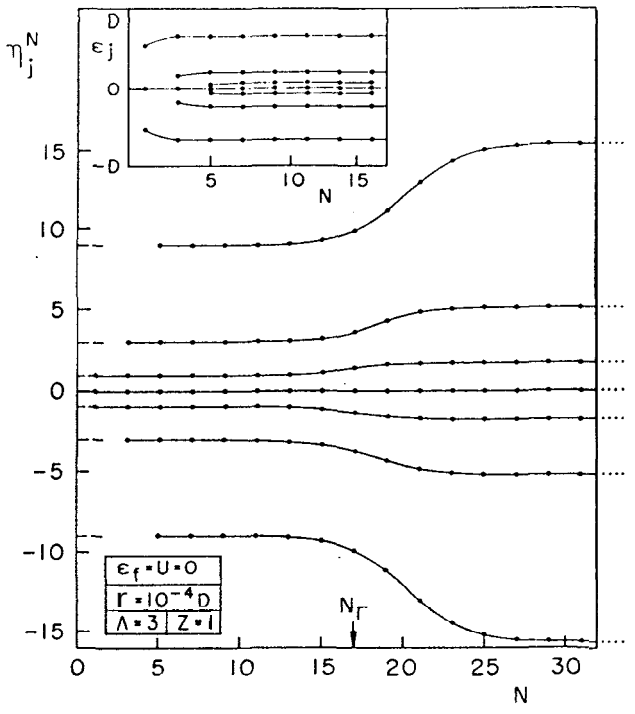

Figure 4.: Eigenvalues of the matrix $\mathcal{H}_N$, defined by Eqs. (27) and (28), for V = 0.01 and **A** = **3.** The eigenvalues are plotted as functions of (odd) N. For N = 1 and **3,** all eigenvalues appear. For N ≥ 5, only the 5 ones closest to the Fermi level are shown. The dashed lines indicate the (odd N) eigenvalues for V = 0, and the dotted lines the eigenvalues for V → ∞. The inset shows the energy levels—equal to the eigenvalues of H_N multiplied by the scaling factor D_N—as functions of N. As N → N + 2, two additional eigenvalues ϵ_j appear close to the Fermi level (for N ≥ 7, these new eigenvalues are so close to zero that they cannot be distinguished from the eigenvalue $\epsilon_j = 0$ on the scale of the plot). For increasing N the discrete eigenvalues thus probe of the vicinity of the Fermi energy with progressively finer resolution.

in the conduction band. On the main plot, the dashed lines are those levels, scaled according to Eq. (29).

As N grows, the diagonalization probes progressively smaller energies ϵ. Eventually, ϵ becomes small in comparison with the width Γ. At this point, letting V → ∞ in Eq. (24) should be a good approximation. The characteristic energy Γ then diverges, making the Hamiltonian H_N again invariant under scaling, i. e., a fixed point. The dotted lines coming to the right-hand vertical axis on Figure 4 coincide with the eigenvalues $\hat{\eta}_j$ of the Hamiltonian in Eq. (24) diagonalized for very large V. Notice that the $\hat{\eta}_j$ are shifted with respect to the eigenvalues for V = Ω This is expected: for Γ → ∞, all conduction levels should be strongly coupled to the impurity, hence phase shifted by $\pi/2$; the displacements of the $\hat{\eta}_j$ relative to the eigenvalues for

N < 10 reflect this phase shift.

The numerical diagonalization thus identifies two fixed point Hamiltonians, obtained from Eq.(24) by setting V = 0 and V = ∞. First found in Ref. 7, these fixed points have been named the *free-orbital* and the *frozen-impurity* fixed points, respectively. Due to the differences between the even-N and odd-N patterns, the eigenvalue structure of either fixed point is repeated under the double transformation $\mathcal{T}^2[H_N] = H_{N+2}$, not under the transformation $\mathcal{T}$. This evidence that the fixed-point Hamiltonians are double-cycled has no practical consequences.

As this discussion of Figure 4 indicates, the diagonalization of a model Hamiltonian by the renormalization-group approach locates fixed points of the renormalization-group transformation. The fixed points are usually simple Hamiltonians constituted of non-interacting quasi-particles decoupled from impurity levels. Quite independently from its ability to determine thermodynamical or excitation properties, therefore, the renormalization-group approach gives insight into the physical properties of impurity models.

VI. Thermodynamical Properties

A. Computational Procedure

The iterative diagonalization of a model Hamiltonian was described in Section . Given a small constant a , each iteration N corresponds to a thermal energy $k_BT = D_N/\alpha$ [see Eq. (17)], and the truncated Hamiltonian was divided by D_N to make its smallest eigenvalues of the order of unity.

The net result of iteration N is a band of eigenvalues ranging from unity to E_{∞} —corresponding to energies ranging from D_N to E_{∞} D_N. The Boltzmann weights of the largest energies in this band are of the order of $\exp(-E_{max}D_N/k_BT) = \exp(-E_{max}/\alpha)$, hence negligible, so that the eigenvalues above E_{∞} (which are not calculated) would contribute insignificantly to the thermodynamical averages.

The weights of the smallest energies, on the other hand, are of the order of $\exp(-D_N/k_BT) = \exp(-\alpha)$. Since α is small, the weights of the (scaled) eigenvalues smaller than unity (which are not calculated in iteration N) are approximately equal to 1, so that those eigenvalues can be equated to zero. For a proof of this statement, based on a perturbative treatment of the first Lanczos coefficient neglected in Eq. (18) (i. e., of the coefficient ϵ_N^2), see Refs. 6, 7.

The iterative diagonalization classifies the eigenstates by spin (and by charge). It is then a simple matter to compute the impurity contribution to the magnetic susceptibility, given by

$$\chi_{imp} = (g\mu_B)^2/k_BT\left[\langle S_z^2\rangle - \langle S_{z0}^2\rangle\right], \qquad (30)$$

where the brackets $\langle\rangle$ indicate thermal averaging, S_z denotes the z component of the total (impurity plus conduction electrons) spin and S_{z0} that of a free electron gas (i. e., of a pure conduction band), g is the electronic gyromagnetic ratio, and μ_B is the Bohr magneton.

Likewise, the impurity contribution to the specific heat is

$$C_v = k_B\,(D_N/k_BT)^2\left[\langle H_N^2\rangle - \langle H_{0N}^2\rangle\right], \qquad (31)$$

where H_{0N} is the scaled Hamiltonian for the free conduction band.

B. Flow Diagram for the Symmetric Anderson model

The temperature-dependent impurity susceptibility for the spin-degenerate Anderson Hamiltonian (1-3) was computed by Krishna-murthy et al.[7,25]. Ref. 7 considered the ***symmetric*** model, defined by the condition $\epsilon_f = -U/2$, which makes the impurity — and hence the Hamiltonian — particle-hole symmetric, i. e., invariant under the transformation $c_f \rightarrow c_f^{\dagger}$. The asyrnmetric model was studied in Ref. 25.

The flow diagram for the symmetric model is shown in Figure 5. Of special interest are the three fixed points, indicated by filled squares. Two of them, the free-orbital ($\Gamma = U = \epsilon_f = 0$) and the frozen-impurity ($U = \epsilon_f = 0$, and $\Gamma = \infty$) Hamiltonians, have been discussed in Section V. For $U = \epsilon_f = 0$, the flow in Figure 5 is restricted to the vertical axis. The free-orbital fixed point is unstable, so that even a very small width Γ will drive the scaled Hamiltonian to the frozen-impurity fixed point, as illustrated by Figure 4.

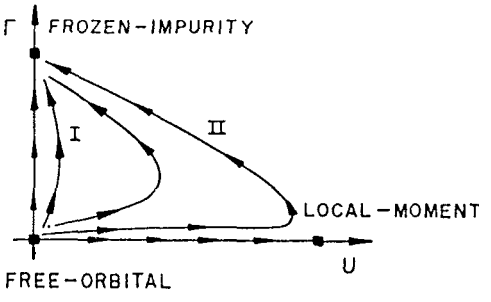

Figure 5.: Flow diagram for the symmetric Anderson model. The free-orbital fixed point is the model Hamiltonian for vanishing impurity-orbital width Γ and Coulomb repulsion U; this fixed point is unstable with respect to Γ and U perturbations. For $\Gamma = 0$ with $U \rightarrow \infty$, the Hamiltonian turns into the local-moment fixed point, unstable with respect to Γ perturbations. For $\Gamma \rightarrow \infty$ with $U = 0$, the Hamiltonian is the (stable) frozen-impurity fixed point.

The third fixed point in Figure 5 corresponds to $U = -2\epsilon_f \rightarrow \infty$, while $\Gamma = 0$. Since V = 0, the impurity is decoupled from the conduction band. Moreover,

$U = \infty$ ($\epsilon_f = -\infty$) makes the doubly-occupied f^2 (the empty f^0) configuration inacessible. The two remaining configurations, $f^\uparrow$ and $f^\downarrow$, are degenerate, which leaves the impurity devoid of characteristic energies. The resulting Hamiltonian is invariant under scaling, that is, a fixed point of the renormalization-group transformation.

In contrast with the free-orbital (four-fold degenerate) and the frozen-impurity (non-degenerate) fixed points, the local-moment fixed point is doubly degenerate, the impurity found in one of its two magnetic configurations, $f^\uparrow$ or $f^\downarrow$. This residual degeneracy makes the local-moment fixed point unstable: for large, but finite U, and small, non-zero Γ, virtual excitations between the magnetic impurity configurations and the non-magnetic ones are allowed. When the impurity coupling to the conduction band, H_{imp-c}, is treated to second order as a perturbation, the following antiferromagnetic coupling between the impurity spin and the spin of the Wannier state centered at the impurity site results:

$$H'_{imp-c} = -2J \sum_{\mu,\nu} f^\dagger_{0\mu} \vec{\sigma}_{\mu\nu} f_{0\nu} \cdot \vec{S}, \qquad (32)$$

where $\vec{S}$ is the impurity spin operator, the components of the vector $\vec{\sigma}$ are the Pauli matrices ($\vec{\sigma} = \sigma_x \hat{x} + \sigma_y \hat{y} + \sigma_z \hat{z}$), and the coupling J is given by the Schrieffer-Wolff relation

$$J = 4\Gamma / A_\Lambda \pi U. \qquad (33)$$

Here the factor A_Λ is defined as

$$A_\Lambda = (\Lambda + 1) \ln \Lambda / 2(\Lambda - 1); \qquad (34)$$

it converges rapidly to unity in the continuum limit, $\Lambda \to 1$.

C. Kondo Limit

The sum of H'_{imp-c} with the conduction Hamiltonian yields the Hamiltonian

$$H_K = -2J \sum_{\mu,\nu} f^\dagger_{0\mu} \vec{\sigma}_{\mu\nu} f_{0\nu} \cdot \vec{S} + \sum_{\mu,n=0}^{\infty} \epsilon_n^z (f^\dagger_{n,\mu} f_{n+1,\mu} + \text{H. c.}), \qquad (35)$$

first diagonalized by Wilson[6]. This relation between the H_K and the Anderson Hamiltonian was first obtained, on the basis of a canonical transformation valid in the $U \gg \Gamma$ limit, by Schrieffer and Wolff[8].

The flow diagram in Figure 5 shows that the antiferromagnetic coupling in H_K drives the scaled Hamiltonian from the local-moment fixed point to the frozen-impurity fixed point. The coupling constant J, however, does not introduce a relevant energy, but a *marginal* one. To understand this, it is convenient to consider the rate of impurity-spin flips caused by H'_{imp-c}, computed in a golden-rule approximation. To this rate r, which is proportional to $(\rho J)^2$, where $\rho = 1/D$ is the density of conduction states, only contribute the conduction states within $k_B T$ of the Fermi energy, so that r is proportional to the temperature. Thus, although the coupling J introduces the characteristic energy $\epsilon_r = r\hbar$, as the temperature is lowered that energy reduces in proportion to $k_B T$. In the golden-rule approximation, at all temperatures, ϵ_r is smaller than $k_B T$ by exactly the same factor, proportional to $(\rho J)^2$, hence small. In contrast with relevant energies, which expand under renormalization-group transformations, and with irrelevant ones, which diminish, the marginal energy ϵ_r remains invariant.

Marginality, however, is a delicate balance. Energies marginal to leading order in perturbation theory frequently turn out to be either relevant or irrelevant in higher orders. In special, higher-order perturbative calculations[6] and numerical computations[6,7] show that ϵ_r is relevant. Since it grows very slowly under the renormalization-group transformation (21), many iterations in the diagonalization of the model Hamiltonian are required to make it effective; eventually, however, it drives H_N from the local-moment fixed point to the frozen-impurity fixed point. The crossover takes place at the energy

$$\Gamma_K = 2.63 D \sqrt{\rho |J|} \exp(1/\rho J)(1 + \mathcal{O}(\rho J)). \qquad (36)$$

In this expression, the two nonanalytical functions of ρJ on the right-hand side [$\sqrt{\rho|J|}$ and $\exp(1/\rho J)$] are universal, i. e., independent of the band structure.

At the temperature $T = \Gamma_K / k_B$, the impurity–spin-flip rate r equals $k_B T$. For thermal energies smaller than Γ_K, the spin-flip rate is large, as it would be if $J \to -\infty$. The impurity spin is strongly coupled to the spin of the conduction electrons around it and forms a singlet. The spontaneous creation of the characteristic energy Γ_K and the formation of the singlet dominate the physical properties of the model for energies ϵ comparable to, or smaller than Γ_K: thermodynamical properties are universal functions of the ratio $k_B T / \Gamma_K$, and dynamical properties are universal functions of ω / Γ_K.

That in the regime $\epsilon \lesssim \Gamma_K$ the Hamiltonian H_K lies beyond the reach of ordinary diagrammatic expansions, it was recognized long before the diagonalization of the H_K. The first symptomatic divergence was found in Kondo's perturbative calculation of the impurity contribution to the resistivity of a dilute magnetic alloy[1]. After him, H_K is nowadays called the Kondo Hamiltonian. A few years afterward, Abrikosov[33], Suhl [34], and Nagaoka[35] found evidence that the antiferromagnetic coupling between the impurity and the conduction band enhances the density of state near the Fermi level. Γ_K [see Eq. (36)] is the width of that resonance, which used to be named after them (it is now more frequently called the Kondo resonance, hence the symbol Γ_K).

D. Numerical Results

Figure 6 shows two illustrative susceptibility curves for the symmetric model. In both cases, $U = 10^{-3}D = -2\epsilon_f$. For curve *I* the conduction-band–to–impurity coupling is $V = 10^{-3}D$, giving an impurity-level width $\Gamma = 3.1 \times 10^{-4}D$, comparable to U. For curve *II*, in contrast, $V = 2.8 \times 10^{-3}D$ corresponds to $\Gamma = 2.5 \times 10^{-5}D$, much smaller than U. Each plot shows the product $T\chi_{imp}$ as a function of temperature. This presentation of the numerical data is convenient, because fixed points are identified by plateaus [this follows from Eq. (20), which shows that the Boltzmann weights depend only on the eigenvalues of the scaled Hamiltonian H_N, which are independent of N at fixed points].

The two plateaus in curve I, the ordinate approximately equal to 0.125 for $k_BT > 10^{-3}D$ and approximately equal to zero for $k_BT < 10^{-5}D$, correespond to the free-orbital and to the frozen-impurity fixed points, respectively. In this case, Γ comparable to U, the scaled Hamiltonian never comes close to the local-moment fixed point. For thermal energies large compared to Γ or U, the impurity energies are unimportant, all four impurity configurations are thermally accessible, and the average $\langle (S_z^{imp})^2 \rangle$ equals 1/8. For thermal energies small compared to Γ, in contrast, only the bonding combination of the impurity orbital with the Wannier state centered at the impurity site becomes thermally accessible. This being non-magnetic, the product $T\chi_{imp}$ vanishes.

In addition to these two plateaus, curve II displays a third one: for $10^{-9}D < k_BT < 10^{-4}D$ the ordinate lies between 0.20 and 0.25. In this range, the scaled Hamiltonian is near the local-moment fixed point. At that fixed point, only the magnetic impurity configurations would be thermally accessible, so that $\langle (S_z^{imp})^2 \rangle$ would equal 1/4. The marginal coupling between the impurity and the conduction band pushes the ordinate somewhat below 1/4. As the temperature is lowered, the marginal energy slowly builds up—as if the coupling J were increasing—and the ordinate drops further below 0.25. At sufficiently low temperatures the impurity–spin-flip rate Γ_K becomes comparable to the thermal energy k_BT. Further lowering of the temperature makes the the impurity spin so strongly coupled to the conduction electrons that its contribution to the product $T\chi_{imp}$ drops to zero.

It was observed above that the crossover from the local-moment to the frozen-impurity fixed point is controlled by the characteristic energy Γ_K, with the result that all thermodynamical properties are functions of the temperature scaled by Γ_K. They are analogous to the thermodynamical properties of the $U = \epsilon_f = 0$ Anderson model, which are functions of the ratio k_BT/Γ. In fact, well before the diagonalization of the Kondo Hamiltonian, a scaling analysis by Toulouse had established an equivalence between the two models at low energies[36]. For thermal energies comparable to or smaller than Γ_K, the thermodynamical properties of the Hamiltonian (35) are remarkably similar to those of the $U = \epsilon_f = 0$ Anderson Hamiltonian with coupling V chosen to make $\Gamma = \Gamma_K$. As an illustration, the dashed line in Figure 6 shows the crossover to the frozen-impurity fixed point in curve I as a function of $(k_BT/D) \times (\Gamma/\Gamma_K)$. The agreement with curve *II* is so close that, on the scale of the plot, for $k_BT < 10^{-11}D$ the two curves cannot be distinguished. A numerical–renormalization-group calculation of the specific heat for the Kondo model found equally good agreement, provided only that the specific heat for H_K be compared with the specific heat per spin for the uncorrelated Anderson Hamiltonian[37].

At thermal energies much lower than the Γ_K, the scaled Hamiltonian is near the frozen impurity fixed point. Here the antiferromagnetic coupling between impurity and conduction electrons around it forms a singlet effectively decoupled from the remaining conduction states. As required by the Friedel sum rule, at the Fermi level the latter are then phase shifted by $\delta = \pi/2$. Since a particle-hole transformation takes the phase shift at the Fermi level from δ to $-\delta$, and since the symmetric Hamiltonian remains invariant under the particle-hole transformation, the only possible phase shifts are $\delta = 0$ and $\delta = \pi/2$ (which is identical to $\delta = -\pi/2$, since the phase shift is only defined $\mathrm{mod}\,\pi$). From this, it is concluded that the Fermi-level phase shift—and hence the low-temperature fixed point that the scaled Hamiltonian approaches—is always the same, independently of the flow of H_N.

The scaled Hamiltonian approaches the frozen-impurity fixed point asymptotically. For large N, the difference between H_N and the fixed-point Hamiltonian can be treated perturbatively, and the impurity contribution to the thermodynamical properties can be calculated analytically[6,7]. For $k_BT \ll \Gamma_K$, the Kondo-resonance width is an irrelevant energy; in the absence of characteristic energies, one expects the thermodynamical properties to be powers of the ratio k_BT/Γ_K. The perturbatively derived expressions for the impurity contributions to the low-temperature magnetic susceptibility and the specific heat are

$$\chi_{imp} = (g\mu_B)^2/2\pi\Gamma_K, \tag{37}$$

and

$$C_{imp} = (\pi/3)k_B^2T/\Gamma_K. \tag{38}$$

When the latter expression is compared with the specific heat of a simple metal, $C = \pi^2k_B^2T\rho_F/3$ [22], where ρ_F is the density of states at the Fermi level, the result is an effective Kondo-resonance density of states

$$\rho_K = 1/\pi\Gamma_K. \tag{39}$$

This confirms that the coupling to the magnetic impurity in the Kondo Hamiltonian introduces a resonance of width Γ_K, just as the coupling to the impurity level

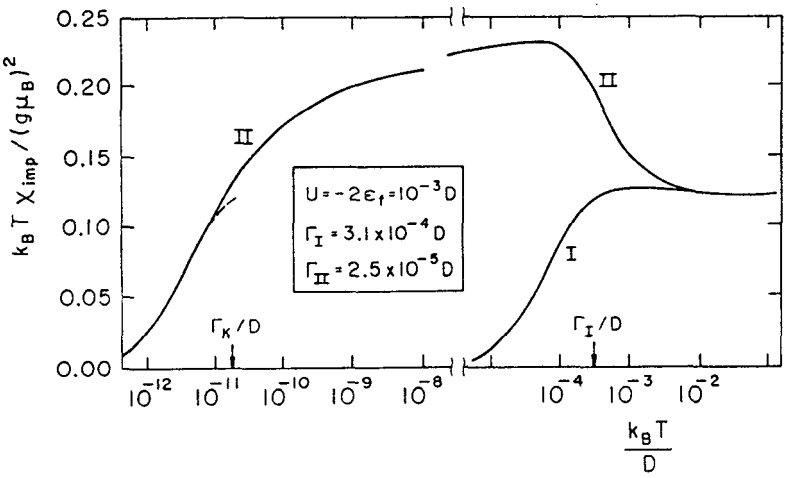

Figure 6.: Magnetic susceptibility for the spin-degenerate syrnrnetric Anderson model, from Ref. 7. The impurity contribution to the susceptibility is multiplied by the temperarture, so that fixed points of the renormalization-group transformation appear as plateaus. At the free-orbital fixed point, the ordinate would equal 1/8; at the local-moment fixed point, 1/4; at the frozen-impurity fixed point, it would vanish. Two plots are shown, both for $U = -2\epsilon_f = 10^{-3}D$, the impurity-level width being $\Gamma_I = 3.1 \times 10^{-4}D$ for curve I and $\Gamma_{II} = 2.5 \times 10^{-5}D$ for curve *II*. Since Γ_I is comparable to U, in case I the scaled Hamiltonian flows directly from the local-moment fixed point to the frozen-impurity fixed point. In case II, it flows first to the vicinity of the local-moment fixed point and then to the frozen-impurity fixed point. The dashed line shows the crossover in curve I displaced horizontally by the factor Γ_K/Γ_I, to show that Γ_K defines an effective resonance width.

in the $U = \epsilon_f = 0$ Hamiltonian introduces a resonance of width Γ. Nonetheless, if from Eq. (39) and from the expression for the Pauli susceptibility of a simple metal, $\chi = (g\mu_B)^2\rho_F/4$ [22], one tries to obtain the low-temperature susceptibility for the Kondo Hamiltonian, the result $[\chi = (g\mu_B)^2/(4\pi\Gamma_K)]$ is only one half the right-hand side of Eq. (37). To emphasize this point, which indicates that the Kondo resonance enhances the magnetic configurations of the conduction states relative to the non-magnetic configurations, Wilson[6] defined the ratio

$$R_W \equiv (4\pi^2/3)[k_B^2 T/(g\mu_B)^2]\chi_{imp}/C_{imp} = 2, \quad (40)$$

in contrast with simple metals, or with the uncorrelated Anderson model, for which $R_W = 1$. Yamada and Yosida later showed that this equality follows from Ward identities in a diagrammatic expansion in the $U \to \infty$ limit[38], while Nozières, on the basis of Fermi-liquid theory, proved that $R_W = 2$ follows from the requirement that the thermodynamical properties of the model remain invariant under infinitesimal shifts of the Fermi level[39]. The Bethe *ansatz* and the $1/N$-expansion solutions of the Kondo problem have generalized Eq. (40) to larger orbital degeneracies. For impurity degrneracy $2S + 1$, the Wilson ratio, defined

$$R_W = [\pi^2/S(S+1)][k_B^2 T/(g\mu_B)^2]\chi_{imp}/C_{imp}, \quad (41)$$

is given by[9]

$$R_W = (2S+1)/2S; \quad (42)$$

only for small degeneracies is it significantly different from unity.

E. Asymmetric Anderson Model

In the symmetric spin-degenerate model, the f^0 and f^2 impurity configurations are degenerate. The asymmetric Hamiltonian breaks this degeneracy, the splitting $A = \epsilon_f + U$ between the f^2 and the f^1 configurations being different from $-\epsilon_f$. Thus, while in the syrnrnetric model U, ϵ_f, or A set the same scale, in the asymmetric case ϵ_f and A are two characteristic energies. The parametrical choice $\Gamma = A = 0$ with $\epsilon_f = -\infty$—a combination not allowed by the symmetric model—makes the Hamiltonian invariant under scaling, since the impurity is decoupled from the conduction band and devoid of characteristic energies. The resulting scaled Hamiltonian is called the *valence-fluctuation* fixed point, a nomenclature attentive to the unequal valentes of the degenerate f^2 and f^1 configurations. Of course, the opposite extreme, $\Gamma = \epsilon_f = 0$ with $A = \infty$, is equally important; as it has been shown[25], however, a particle-hole transformation interchanges the f^0 and f^2 configurations, so that a complete study of the asymmetric model requires only analysis of the parametrical half-space $A > -\epsilon_f$.

The valence-fluctuation fixed point is unstable. It is easy to recognize that any positive A will grow under scaling and drive the scaled Hamiltonian towards the local-moment fixed point. Nevertheless, in analogy with the formation of the characteristic energy

(Γ_K) in the symmetric Hamiltonian, a characteristic energy is generated in the crossover between the valence-fluctuation and the frozen-impurity fixed points. Under the assumption $U + 2\epsilon_f \gg \Gamma$, a perturbative treatment identifies the energy A* determined by the transcedental equation[40,25]

$$A^* = A - \Gamma/\pi \ln |\epsilon_f/\Delta^*| . \quad (43)$$

A*, the effective splitting between the f^2 and the two f^1 configurations, can be significantly different from A. To show this, Figure 7 plots both sides of Eq. (43), divided by Γ, as functions of Δ^*/Γ for $\epsilon_f = -0.1D$, $\Gamma = 0.01D$ and three Δ's: (a) $-0.05D$, (b) 0.0050, and (c) 0.050. For $A = \epsilon_f$, i e., $U = 0$ (not shown), Eq. (43) would admit a single solution, $A^* = A$. For fixed ϵ_f and Γ, however, as A (i. e., U) grows, A* becomes progressively smaller than A. For case (a), the difference be'tween the renormalized splitting and the bare one is insignificant. In case (b), however, while A is positive, A* is negative. In fact, as the figure indicates, Eq. (43) always admits a negative solution, which approaches zero as A becomes much larger than Γ. Under these circumstances, A* can be neglected on the left-hand side of Eq. (43), which shows that

$$A^* = \epsilon_f \exp(-\pi\Delta/\Gamma). \quad (44)$$

This is precisely what the exponential on the right-hand side of Eq. (36) —which defines the width of the Kondo resonance— yields when the Schrieffer-Wolff transformation is carried out on the asymmetric Hamiltonian[8,25]. For $A \gg \Gamma$, therefore, the characteristic energy A* defines a Kondo resonance, just as in the symmetric model.

Figure 7 sliows that for $A > \Gamma$ Eq. (43) has two additional, positive roots. One of them —the one closest to zero— is approximately the symmetric of the solution in Eq. (44); this is again the Kondo resonance, which is centered at the Fermi level and therefore spreads to both positive and negative energies. The other root is $A^* \approx A$.

In summary, as long as $|\Delta| \gg \Gamma$, there is always a cliaracteristic energy A* approximãtely equal to the bare splitting A; for $A < 0$, the nonmagnetic configuration f^2 predominating in the ground state, that energy controls the crossover from the valence-fluctuation to the frozen impurity fixed point. For $A > 0$, in contrast, the magnetic f^1 configurations are predominant, and the crossover occurs in two stages: as k_BT approaches A, the scaled Hamiltonian is driven from the valence-fluctuation to the local-moment fixed point; further reduction of the temperature makes k_BT comparable to, and then smaller than $A^* = |\epsilon_f| \exp(-\pi\Delta/\Gamma)$ and drives H_N from the local-moment to the frozen-impurity fixed point. For $|\Delta| \lesssim \Gamma$, on the other hand, the crossover is controlled by the energy scale in Eq. (43). These features, first identified in the impurity magnetic-susceptibility curves in Ref. 25, appear more clearly on the spectral-density plots discussed in Section VIII.

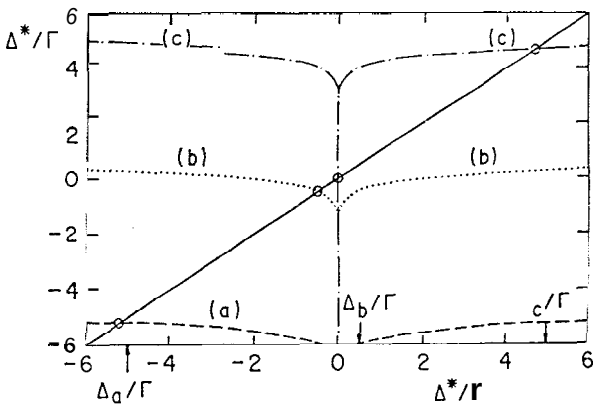

Figure 7.: Graphical solution of Eq. (43). Both sides of that relation, divided by Γ, are plotted as functions of Δ^*/Γ for $\Gamma = 0.010$, $\epsilon_f = -0.1D$, and three $f^1 - f^2$ splittings: (a) $A = -0.050$, (b) $A = 0.0050$, and (c) $A = 0.050$, which correspond to the three parametrical choices in Figure 8. The solutions of Eq. (43) are identified by circles. Cases (a) and (b) have one solution each, with $A^* < 0$. Case (c), $A = 5\Gamma$, has three solutions. As discussed in the text, the two roots closest to zero reflect the Kondo resonance; the third one shows that, as in case (a), for $|\Delta| \gg \Gamma$ there is always a solution with $A^* \approx A$.

F. Extensions of the Anderson Hamiltonian

Renormalization-group calculations of thermodynamical properties for extensions of the Anderson model have been carried out by various authors. Allub et al.[41] pioneered a study of a model[42] with two magnetic configurations: conduction-band-to-impurity charge transfer augments the impurity spin from $S = 1/2$ to $S = 1$. The Hamiltonian is rotationally invariant. The impurity takes different energies, $E_{1/2}$ or E_1, depending on its spin. This model describes crudely compounds of such rare-earth ions as Tm, whose two lowest configurations ($4f^{12}$ and $4f^{13}$) are magnetic and some of whose compounds seem to have a magnetic ground state[43]. The fixed-point structure of the model Hamiltonian is similar to that of the Anderson Hamiltonian. A valence-fluctuation fixed point, two local-moment (with $S = 1/2$ and $S = 1$, respectively) fixed points, and a frozen-impurity fixed point are found. Near the valence-fluctuation fixed point the energy splitting $A = E_1 - E_{1/2}$ is renormalized as in Eq. (43). Unlike the ground state of the Anderson Hamiltonian, however, the ground state of the Hamiltonian studied in Ref.41 is doubly degenerate: tlie conduction

electrons around the impurity couple antiferromagnetically to it and reduce its maximum spin from $S = 1$ to $S = 1/2$. At low temperatures ($k_B T$ smaller than any energy scale), then, the magnetic susceptibility follows the Curie law.

This conclusion seems inevitable for a model in which the orbital degeneracy of the conduction electrons is smaller than that of the impurity. A more realistic model, with orbitally degenerate conduction electrons, has been formulated[44]. That model cannot be diagonalized by the Bethe ansatz. $1/N$ expansions have been carried, indicating that the ground state is nondegenerate[44,45], a result supported by the renormalization-group calculation of the magnetic susceptibility by Shimizu et al.[46]. More recently, however, on the basis of a narrow-band (or strong-coupling) approximation. Baliña and Aligia have concluded that the ground state is nonmagnetic only for $j - j$ coupling, a magnetic ground state resulting from Russel-Saunders coupling[47].

Another extension of the Anderson Hamiltonian considered a localized (i. e., momentum-independent) electrostatic interaction G between the impurity-orbital charge and the conduction electrons[48,49]. This potential phase shifts the conduction states and therefore modifies the conduction-band energy. Since the strength of the potential depends on the impurity occupation, G affects the thetmodynamical properties by modifying tlie splittings ϵ_f and **A** between the $4f^0$ and $4f^1$ and between the $4f^1$ and the $4f^2$ configurations, respectively. The differences between the calculated susceptibility curves for $G \neq 0$ and those for $G = 0$ are minor[48]. Frota and Mahan[49] (who calculated the ground-state impurity occupation) nevertheless find that, for $G \approx U$, the Coulomb repulsion $U > 0$ can become effectively negative, $U \rightarrow U_{eff} < 0$. The consequerices of this pairing interaction remain to be explored.

VII. Diagonalizations of Model Hamiltonians

A. General Aspects

Section IV presented the iterative procedure that diagonalizes the spin-degenerate Anderson Hamiltonian. Only minor modifications are required to adapt the technique to more complex impurity Hamiltonians, but the computational cost increases so steeply with the degeneracy of the orbitals and with the number of impurities that only a few more general models have been investigated.

As pointed out in Section IV C, in the diagonalization of the spin-degenerate Anderson Hamiltonian, the number of basis states n_b required in iteration N to compute thermodynamical properties is approximately independent of N. That number turns out to be a few hundred, so that when the basis is divided into independent subspaces classified by charge and spin, the largest matrices that must be diagonalized are of dimension 100.

Unfortunately, orbital degeneracy augments those numbers enormously. It was shown in Section IV C that each Lanczos operator $f_{n\mu}$ multiplied the number of basis states by a factor of 2. For spin degeneracy and fixed n, the operators are two ($f_{n\uparrow}$ and $f_{n\downarrow}$), so that each f_n introduces a factor of 4. For N_J-degenerate electrons, each operator introduces a factor 2^{N_J} instead of 4. Similarly, the number of basis states in each iteration increases from $n_b \approx 300$ to $n_b^{N_J/N_S}$. Even for $N_J = 6$, corresponding to orbital degeneracy $N_L = 3$, the number of states will be enormous — tens of millions. Exactly the same problem appears in many-impurity computations: for spin-degeneracy, for instance, the number of basis states grows from n_b to $n_b^{N_i}$, where N_i is the number of impurities. For two impurities, the number of basis states would be close to 100,000.

Such calculations are obviously impossible, and the renormalization-group approach would seem applicable only to one impurity and spin-degenerate electrons. However, if instead of computing thermodynamical (or excitation) properties one is content with diagonalizing a model Hamiltonian, the procedure has a broader scope. Since the Boltzmann factor is then immaterial, the upper bound E_m of the band of energies kept in each iteration can be substantially reduced. The number of basis states is likewise reduced, ten-fold for the single-impurity spin-degenerate problem, a hundred-fold for the two-impurity model. If the calculation of excitation properties for a given model will not fit in one's computational budget, diagonalizing the model Hamiltonian is an attractive alternative.

To this expedient first resorted Cragg and Lloyd[50]. They studied two generalizations of the Kondo Hamiltonian diagonalized in Ref. 6, introducing (i) a potential scattering term $G\sum_\mu f_{0\mu}^\dagger f_{0\mu}$, (ii) a spin-S impurity ($S \geq 1/2$) coupled to one or two channels of spin-1/2 electrons. The former modification turns out to be unimportant, for the potential scattering merely phase shifts the conduction electrons. The latter, however, showed that a single channel of spin-1/2 electrons are unable to compensate the larger impurity spin, so that the ground state has spin $S - 1/2$. When two channels are considered, for $S > 1/2$ the ground state has spin $S - 1$, which indicates that each channel subtracts 1/2 from tlie impurity spin. For $S = 1/2$, with two channels there is overscreening: the degenerate channels combine to form two sets of free electrons: one phase-shifted by $\pi/2$ (an electron from this set having formed a singlet with the impurity) and the other not phase-shifted. Ref. 50 provided testgrounds for Nozières's and Blandin's general discussion of orbitally degenerate magnetic impurities in metals[51], whose findings were a few years later confirmed and complemented by

Bethe *ansatz* computations of thermodynamical properties for the generalized Kondo Hamiltonian[8]. Interest in the case $S = 1/2$ with two electron channels was revived by the recent suggestion[52] that crystal-field effects might give rise to a quadrupolar Kondo effect in uranium heavy-fermion compounds (such as UPt_3), which is equivalent to that overscreened model. Consequently, a renormalization-group calculation oriented towards high accuracy was combined with a conforma1 field-theoretical analysis of that problem to bear out and to extend (e. g., by including a magnetic field) the earlier conclusions[53].

Another, rather original application of the numerical renormalization group procedure is reported in Ref. 54, which takes advantage of the (approximate) equivalence[55] between the single-impurity Anderson Hamiltonian and a model Hamiltonian describing the Coulomb blockade in mesoscopic tunnel junctions to calculate the ground-state energy for the latter. That work is mentioned only in passing, as it lies off the mainstream of this review.

B. Two-Impurity Kondo Problem

The clearest demonstration that the renormalization group diagonalization of a model Hamiltonian is sufficient to give quantitative insight into its basic properties was provided by Jones et al.[14–16], who have studied the two-impurity Kondo model. That problem has a long history, dating back to the work of Alexander and Anderson[56] on interacting localized states in metal ~Instead of one, the model considers two impurities in a metallic environment, separated by a distance R. Each of them is coupled antiferromagnetically to s-wave conduction states centered at the impurity site. The full Hamiltonian is

$$H_{II} = \sum_{k,\mu} \epsilon_k c^\dagger_{k\mu} c_{k\mu} - J \sum_{\mu,\nu} \psi^\dagger_\mu(\vec{R}/2)\psi_\nu(\vec{R}/2)\vec{\sigma}_{\mu\nu}\cdot\vec{S}_1 - J \sum_{\mu,\nu} \psi^\dagger_\mu(-\vec{R}/2)\psi_\nu(-\vec{R}/2)\vec{\sigma}_{\mu\nu}\cdot\vec{S}_2, \qquad (45)$$

where $\vec{S}_1$ and $\vec{S}_2$ are the impurity spins at sites $\vec{R}/2$ and $-\vec{R}/2$, respectively, and the fermionic operator $\psi(\vec{r})$ annihilates an electron in the Wannier state centered at position $\vec{r}$.

If the two impurities were infinitely apart, the Harniltonian (45) could be separated into two single-impurity problems, each impurity interacting with its surrounding electrons. Because R is finite, this separation is impossible, because the Wannier operators $\psi(\vec{R}/2)$ and $\psi(-\vec{R}/2)$ are non-orthogonal. To ensure orthogonality, one works with odd and even linear combinations of the s-wave conduction states centered around each impurity site. The result is that the discretized conduction-band Hamiltonian [analogous to Eq.(10)] has the form

$$H_c = \sum_{\mu,n=0}^{\infty} \epsilon^z_n (f^\dagger_{n,\mu,o} f_{n+1,\mu,o} + f^\dagger_{n,\mu,e} f_{n+1,\mu,e} + \text{H. c.}), \qquad (46)$$

where the subscripts o and e indicate odd and even operators, respectively.

The coupling to the impurity is

$$H_{imp-c} = -(\vec{S}_1 + \vec{S}_2)\cdot\sum_{\mu,\nu}\left(J_e f^\dagger_{0e\mu}\vec{\sigma}_{\mu\nu} f_{0e\nu} + J_o f^\dagger_{0o\mu}\vec{\sigma}_{\mu\nu} f_{0o\nu}\right) - (\vec{S}_1 - \vec{S}_2)\cdot\sum_{\mu,\nu}\left(\sqrt{J_o J_e} f^\dagger_{0e_\mu}\vec{\sigma}_{\mu\nu} f_{0o\nu} + \text{H. c.}\right), \qquad (47)$$

where

$$J_e = [(1+S)/2]J, \qquad (48)$$

and

$$J_o = [(1-S)/2]J, \qquad (49)$$

with

$$S = \sin(k_F R)/k_F R. \qquad (50)$$

To obtain Eq. (47), it is necessary to substitute the Fermi momentum k_F for the absolute value of the electronic mornentum k in the exponentials $\exp(\pm i\vec{k}\cdot R)$ that appear when the field operators $\psi(\pm\vec{R}/2)$ on the right-hand side of Eq.(45) are expressed as linear combinations of the conduction states $c_{\vec{k}}$. As a consequence of this substitution, the Hamiltonian (47) depends on R only through S, so that infinitely separated impurities become identical to impurities separated by the distance $R = \pi/k_F$. The approximation $k \to k_F$ is nevertheless justified, for it neglects only irrelevant terrns of the model Hamiltonian.

Equation (46) associates with each Lanczos coefficient ϵ^z_n four kinds of fermionic operators: $f_{n\uparrow o}$, $f_{n\downarrow o}$, $f_{n\uparrow e}$, and $f_{n\downarrow e}$, in contrast with the two kinds ($f_{n\uparrow}$ and $f_{n\downarrow}$) in the single-impurity problem. For this reason, as pointed out in Section VII A, if n_b is the number of states that have to be kept in an iterative diagonalization of the single-impurity Hamiltonian, $(n_b)^2$ will be the number needed to diagonalize the two-impurity Hamiltonian. To reduce the dimensions of the matrices that have to be diagonalized, in addition to the conservation laws of the single-impurity problem, one takes advantage of parity conservation.

It has long been realized that the two-impurity problem is richer than the single-impurity one[57]. While the latter has a single characteristic energy scale (the Kondo energy), the former has two: the Kondo width Γ_K and the RKKY dipolar coupling between the impurity spins. This coupling, an interaction mediated by the conduction electrons, has the form

$$H_{RKKY} = -I_0 \vec{S}_1\cdot\vec{S}_2, \qquad (51)$$

where[16]

$$I_0 = 2 \ln 2 \rho (J_e - \mathrm{J},)^2 . \qquad (52)$$

The cornpetition between I_0 and $k_B T_K$ governs the physics of the model. Two stable fixed points have been identified. For $I_0 \rightarrow -\infty$, the (antiferromagnetic) RKKY interaction in Eq. (51) couples the two impurity spins so strongly that they form a singlet effectively decoupled from the conduction band. The scaled Hamiltonian therefore reduces to the conduction-band Hamiltonian, a fixed point of the renormalization-group transformation called the ***coupled-impurities*** fixed point. If, on the other hand, $I_0 = 0$ and $J \rightarrow -\infty$, each impurity couples strongly to the conduction electrons around it; as in the single-impurity problem, each conduction-band channel is phase shifted by $\pi/2$. The scaled Hamiltonian is again a fixed point of the renormalization-group transformation, the *frozen-impurities* fixed point. The different conduction-state phase shifts distinguish the coupled-impurities fixed point from the frozen-impurities fixed point.

The numerical results show that, for $I_0 > -2.2 k_B T_K$, the ground state is the frozen-impurities fixed point, i. e., the Kondo effect wins over the RKKY interaction. For $I_0 < -2.2 k_B T_K$, the ground state is the coupled-impurities fixed point, indicating that the antiferromagnetic coupling between the impurity spins locks them into a singlet before they can couple to the conduction electrons.

At the boundary between the two domains (i. e., for $I_0 = -2.2 k_B T_K$) lies an unstable fixed point with the characteristics of a second-order phase transition: the linear coefficient of the specific heat and the staggered magnetic susceptibility diverge[15]. As in the theory of critical phenomena, this fixed point results from the balanced competition between the two stable fixed points. The discovery of this fixed point raised a temporary controversy, for Monte Carlo computations found the staggered susceptibility to be finite[58]. A very recent conformal-mapping analysis[59] has nevertheless confirmed tlie numerical renormalization group result.

At any rate, the unstable fixed point seems of limited physical interest, since a more general renormalization-group study including potential scattering has sliown that the breaking of the particle-hole symmetry of the Kondo Hamiltonian washes it out[16].

VIII. Excitation Properties

A. Computational Procedure

To calciilate ground-state and thermodynamical properties, the $z = 1$ discretization of the conduction band — introduced in Ref. 6 — is sufficient. To compute excitation properties, however, the second discretization parameter is indispensable. As an illustration, consider the impurity spectral density ρ_f(c) for the Anderson model. For given r, the golden rule gives:

$$\rho_f(\epsilon)^z = \begin{cases} \sum_{F,\mu} |\langle F|c_{f\mu}|\Omega\rangle|^2 \delta(E_F^z - E_\Omega^z - \epsilon) & (\epsilon > 0) \\ \sum_{F,\mu} |\langle F|c_{f\mu}^\dagger|\Omega\rangle|^2 \delta(E_F^z - E_\Omega^z + \epsilon) & (\epsilon < 0) \end{cases} \qquad (53)$$

where c is the binding energy, $|\Omega\rangle$ the ground state (energy E_Ω), and $|F\rangle$ is any eigenstate of the Hamiltonian (1) (energy E_F). Interest in this function arises because laboratories have direct access to it: for positive ϵ, the spectral density is measured by X-ray Photoemission Spectroscopy (XPS); for negative ϵ, by inverse photoemission, or Bremstrahlung Isochromat Spectroscopy (BIS).

Once the eigenvalues and eigenstates of the Anderson Hamiltonian have been computed by the iterative procedure in Section IV, it is a simple matter to compute the sums on the right-hand side of Eq. (53). Nonetheless, given the discretization of the conduction band, only discrete energy differences $E_F^z - E_\Omega^z$ satisfy the energy-conservation condition imposed by the delta function. The golden rule, which describes transitions to a continuum, is inapplicable. Should one insist on calculating the spectral density from Eq. (53), spiked spectra strongly dependent on the discretization parameter **A** and bearing no resemblance to experimental data would result.

Early attempts to improve such computations employed convolutions on the logarithmic energy scale. Two convolution functions have been proposed, both of width ln **A**, equal to the separation between successive energies in Figure 3: (i) a box[60], and (ii) a Gaussian[61,62]. In most cases, these procedures were employed to calculate excitation properties near fixed points, where they can be justified (see below). Away from fixed points, however, not only are they unjustified, but they have been shown[31] to severely underestimate the spectral density. In particular, since the impurity spectral densities for the Anderson and for more complex Hamiltonians exhibit salient features at crossovers, numerical renormalization group calculations involving convolutions of their excitation properties are unreliable, even semi-quantitatively.

The difficulty with crossovers is easily understood. The discretization in Figure 3 affects only the conduction band, not the impurity states. The model Hamiltonian is subsequently diagonalized. The resulting eigenvalues and eigenstates are in general combinations of impurity and conduction states, so that impurity and conduction states contribute to the discrete spectral density in **Eq.** (53). Since the convolution can make no distinction between impurity and conduction states and since it is based on the discretization of the conduction band, it ends up broadening unduly the impurity levels — broadening them as if they were discrete conduction states. Near fixed points, where the scaled Hamiltonian contains no characteristic energies, this

problem is immaterial; at crossovers, however, where the impurity levels constitute the characteristic energies, resonances are invariably widened. Their peak intensities are proportionally reduced, since the convolution preserves the spectral weight of a resonance. A study of the analytically soluble $U = 0$ Anderson model has shown that with standard choices of the parameters Γ and ϵ_f, and either the box or the Gaussian functions, the convoluted spectral densities at the resonance maximum ($\omega = -\epsilon_f$) can be less than one-half of the exact result[31].

To avoid such alarming deviations, one takes advantage of the second discretization parameter. As z varies from 0 to 1, the discrete energies in Figure 3 run through every conduction energy. With z a variable in that range, the conduction-band continuum is recovered. Accordingly, the impurity spectral density is obtained by integrating Eq. (53) over z:

$$\rho_f(\epsilon) = \int_0^1 \rho_f^z(\epsilon)\, dz, \tag{54}$$

which yields

$$\rho_f(\epsilon > 0) = \sum_{F,\mu} |\langle F|c_{f\mu}|\Omega\rangle|^2 / |d\mathcal{E}/dz|\big|_{\mathcal{E}=\epsilon}, \tag{55}$$

where $\mathcal{E} = \mathcal{E}(z) = E_F^z - E_\Omega^z$. A similar expression results for $\omega < 0$. In numerical computations, the integration on the right-hand side of Eq.(54) is carried out on a mesh of ten equally spaced z's, and the derivative in the denominator on the right-hand side of Eq. (55) is evaluated numerically.

At a fixed point, that derivative turns out to equal $-\mathcal{E}\ln\Lambda$ [31]. With this result substituted in Eq. (55), the box convolution[60] is recovered, thus providing justification for that procedure. At crossovers, however, impurity levels contribute to $\mathcal{E}$; since the impurity energies are independent of **A**, the denominator on the right-hand side of Eq. (55) in general is significantly smaller than $\mathcal{E}\ln\Lambda$. Spectral densities calculated from Eq. (55) can therefore be substantially larger than the convoluted densities. For $U = 0$ (and both $|\epsilon_f|$, and Γ much smaller than the bandwidth), a straiglitforward analysis[31] shows that

$$\rho_f(\epsilon) = (2/\pi\bar{\Gamma})/[\bar{\Gamma}^2 + (\epsilon + \epsilon_f)^2], \tag{56}$$

where $\bar{\Gamma} = \Gamma/A_\Lambda$ converges rapidly to Γ as $\Lambda \to 1$. Apart from this multiplicative renormalization of Γ [63], Eq. (56) agrees with the exact result: the spectral density is a Lorentzian of half width at half maximum Γ, centered at the impurity energy ϵ_f.

B. Anderson Model

Figure 8 shows three spectra for the spin-degenerate Anderson model[18,64]. The ordinate is normalized by the maximum density for the U = 0 model, $\rho_f^{max} = 2/(\pi\Gamma)$ [see Eq. (56)]. The spectra have been computed for $\epsilon_f = -0.1D$ and $\Gamma = 0.01D$, and for three splittings between the f^2 and f^1 impurity configurations: (a) $\Lambda = -0.050$ (corresponding to Coulomb repulsion $U = 0.05D$), (b) $\Lambda = 0.005D$ ($U = 0.105D$), and (c) $\Lambda = 0.05D$ ($U = 0.150$). The parametrical choice $|\epsilon_f| \gg \Gamma$ excludes the f^0 configuration from the ground (initial) state. In (a), modest Coulomb repulsion, the ground state occupation n_f is approximately 2. An energy $\omega = -\Lambda$ is necessary to remove an electron from the impurity. Phenomenologically, this Hamiltonian is equivalent to an uncorrelated Hamiltonian with impurity energy $\epsilon_f = -0.05D$. According to Eq. (56), then the spectrum should comprise a resonance with half width at half maximum Γ, centered at

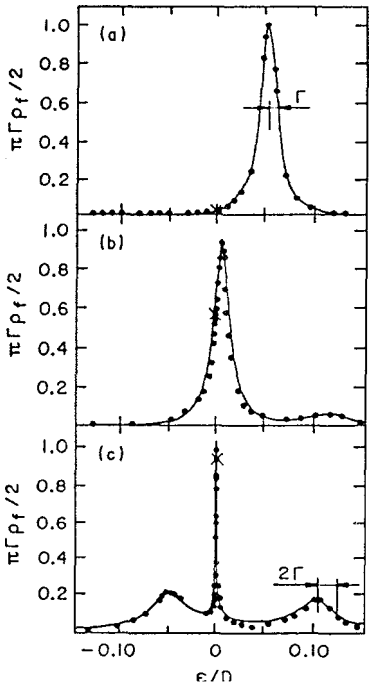

Figure 8.: Spectral density for the spin-degenerate Anderson model, from Ref. 64. The dots are calculated densities; the solid lines in **(a)** and (b) attempt to fit them with Lorentzians of the indicated half widths at half maximum. In (c), the central peak is fitted with Eq. (58), and the satellites with Lorentzians. The crosses at $\omega = 0$ indicate the exact spectral density at the Fermi level, calculated from Eq. (57). For the three cases, $\epsilon_f = -0.1D$ and $\Gamma = 0.01D$. The $f^1 - f^2$ splitting A increases progressively from (a) to (c): A, $= -0.050$, $\Delta_b = 0.005D$, and **A,** $= 0.05D$. The $f^2 \to f^1$ resonance in spectrum (a) is pinned at the Fermi level and narrows into the Kondo resonance as **A** grows and the impurity occupation approaches unity (Kondo limit). The $f^1 \to f^0$ resonance, peaked at $\epsilon \approx |\epsilon_f|$, grows with A, as does the $f^1 \to f^2$ resonance, peaked at $\omega = -\mathbf{A}$.

$\epsilon = -A = (.05D$, in agreement with Figure 8(a).

As U increases, however, this single-particle description fails. For $A \approx 0$, so that $|\Delta| < \Gamma$, the f^1 and f^2 configurations are essentially degenerate, and for $|\epsilon_f| \gg \epsilon \gg \Gamma$ the model is in the valence-fluctuation regime, near the valence-fluctuation fixed point. Here, the ground state combines the f^1 and f^2 impurity configurations, with two consequences: first the photoemission $f^1 \rightarrow f^0$ gives rise to the broad resonance centered approximately at the binding energy $\epsilon = 0.1D = -\epsilon_f$. Since the final state in this transition has *two* decay channels ($f^0 \rightarrow f^\uparrow$ and $f^0 \rightarrow f^\downarrow$), this peak is twice as broad as the one in Figure 8(a) (which has a single decay chanriel, $f^1 \rightarrow f^2$). Compared to the maximum in the first plot, the peak density is significantly smaller both because the resonance is broader and because the final impurity state (f^2) is nondegenerate; while the $f^2 \rightarrow f^1$ density can reach unity on the vertical scale, the spectral density for an $f^1 \rightarrow f^0$ transition can never exceed 0.25.

The second significant difference hetween plots (a) and (b) is the position of the $f^2 \rightarrow f^1$ maximum. In the valence-fluctuation regime, as Section VI E pointed out, the splitting A between the f^1 and f^2 configurations is renormalized to **A*** [Eq. (43)]. In particular (see Figure 7) the parametrical choices in Figure 8(b) make $A^* \approx -5 \times 10^{-3} D$. The positive binding energy $\epsilon = -A^*$—not the negative energy $\epsilon = -A$—is indeed where the sharper resonance in Figure 8(b) peaks. Careful inspection of the plot reveals yet another many-body effect: the fitting of the calculated densities (filled circles) with a Lorentzian of half width at half maximum Γ (solid line) is inferior to the one in Figure 8(a); the resonance has narrowed. As U and A grow further, the $f^2 \rightarrow f^1$ resonance narrows further to a width **A*,** its peak pinned to the Fermi level. Alternatively said, the model eriters the Kondo regime.

The signature of the Kondo limit is the sharp resonance at the Fermi level. That its peak intensity should be $\rho_f(0) = 2/\pi\Gamma$ is the consequence of a rigorous result by Langreth[65], which shows that

$$\rho_f(\epsilon = 0) = (2/\pi\Gamma)\sin^2\delta_F, \qquad (57)$$

where δ_F is the phase shift at the Fermi level, equal to $\pi/2$ in the Kondo limit.

The width of the Kondo resonance is Γ_K [Eq. (36)], approximately equal to **A*.** A decade ago, when insight gained from thermodynamical calculations and various special results were combined into the first description of the impurity spectrum for the spin-degenerate Anderson Hamiltonian[26], a Lorentzian resonance was imagined. The renormalization-group computation in Ref.18 nonetheless found the broadened–Doniach-Šunjić[66] lineshape

$$(1/2)\pi\Gamma\rho_f(\epsilon) = \mathrm{Re}\sqrt{\frac{i\Gamma_K}{\epsilon + i\Gamma_K}}. \qquad (58)$$

A recent quantum–Monte-Caro calculation has been able to reproduce this result[67].

The square root on the right-hand side is due to the response of the conduction electrons to the sudden change of the phase-shift that accompanies the photoemission. At the ground state, the impurity forms a singlet with the conduction electrons around it, and the phase shift δ is $\pi/2$; this is the frozen-impurity fixed point. For energies much larger than Γ_K, however, the scaled Hamiltonian is close to the local-moment fixed point, where the two degenerate f^1 configurations coexist with a free conduction band, phase shift $\delta = 0$. For $\epsilon \gg \Gamma_K$, then, the $f^2 \rightarrow f^1$ transition subjects the conduction-electron phase shift to a variation $\Delta\delta = -\pi/2$. As established by Doniach and Šunjić[66], the electronic response in a normal metal to a sudden change of phase shift (caused by the photoemission of a core electron) makes the core-state spectral density divergent:

$$\rho_{core}(\epsilon) \sim (\epsilon/D)^{g(\Delta\delta/\pi)^2 - 1} \qquad (\epsilon \ll D), \qquad (59)$$

where g is the degeneracy of the conduction states. For spin degeneracy and $\Delta\delta = \pi/2$, Eq. (59) gives

$$\rho_{core}(\epsilon) = (\epsilon/D)^{-1/2}. \qquad (60)$$

Equation (58) shows that Γ_K dampens this singularity, making the spectral density finite at the Fermi level, as required by Eq. (57). For a more extensive discussion of the shape of the Kondo resonance, see Ref. 68.

The satellite peaks in Figure 8(c) are simpler. The hump centered at the binding energy $\epsilon \approx |\epsilon_f| = 0.1D$, is the already discussed $f^1 \rightarrow f^0$ resonance. The feature centered at $\epsilon = -0.050 = -\Delta^*_{max}$ (where Δ^*_{max} is the largest root of the transcedental Eq. (43), visible on curve (c) in Figure 7) is the $f^1 \rightarrow f^2$ resonance, an inverse photoemission. Since the particle-hole transformation [$c_f \rightarrow c_f^\dagger$ and $c_k \rightarrow c_k^\dagger$] turns the latter transition into the former, the two satellites have the same qualitative characteristics. In special, both are Lorentzians with half width at half maximum 2Γ.

The crosses at $\epsilon = 0$ in Figure 8 check the accuracy of the calculation. The Friedel sum rule relates the ground-state impurity occupation n_f to the Fermi-level phase shift δ_F. Given that the Bethe *ansatz* determines n_f [13], the zero-energy spectral density can be computed from Eq. (57). The results, indicated by the crosses, are in exceilent agreement with the calculated densities.

Brito and Frota[69] have calculated the core-level spectral density for the Anderson model. Following Gunnarsson and Schönhammer[27], they have added to the Anderson Hamiltonian a core level from which an electron is photoejected. The resulting core-hole drags the 4f levels below the Fermi level. In addition, they

considered a localized potential G representing the electrostatic interaction between the core hole and the conduction electrons. Once below the Fermi level, the initially empty impurity levels tend to absorb charge from the conduction band; this lowers the conduction-band energy, the balance being transferred to the outgoing core electron. Thus, if the final-state impurity energy is $\epsilon_f < 0$, a resonance centered at ϵ_f should be found in the core-hole spectrum, its width proportional to Γ. In addition, the spectral density should diverge at the Fermi energy according to the Doniach-Šunjić rule, Eq. (59). The spectra calculated in Ref. 69 for $G = 0$ display these expected features. For $G \neq 0$, the low-energy core-hole spectral density still obeys a power law, but the exponent deviates from the Doniach-Šunjić expression. It grows linearly with G and becomes positive—the spectral density vanishing at the Fermi level—for sufficiently large core-hole–conduction-band interaction. At the same time, the width and maximum density of each resonance is significantly dependent on G. The authors conclude that hybridization parameters (Γ) extracted from core-hole photoemission experiment may conflict with the same parameters extracted from other physical properties, a conclusion at variance with the findings of Ref. 27.

Frota[70] has computed the dynamical charge susceptibility for the Anderson model, the Fourier transform of the impurity density-density correlation function, given by

$$\chi_c(\epsilon) = \sum_F |\langle F| \sum_\mu c^\dagger_{f\mu} c_{f\mu} |\Omega\rangle|^2 \delta(E_F - E_\Omega - \epsilon). \quad (61)$$

His results are restricted to the vicinity of the Kondo limit, the ground-state impurity occupation approximately equal to 1. Three calculations are reported, all for impurity-orbital energy $\epsilon_f = -0.1D$, and impurity-level width $\Gamma = 0.01D$. The $f^1 \rightarrow f^2$ splitting Δ in the three computations are $0.2D$, $0.3D$, and $0.4D$, respectively. If Γ were zero, the two-fold degenerate ground state would contain only the f^1 impurity configurations. The spectrum of χ_c would then consist of a single line at the Fermi level, corresponding to the final-state impurity configuration f^1. For non-zero Γ, the degeneracy of the f^1 configurations is broken at an energy $\epsilon \approx \Gamma_K$. The Kondo resonance thus formed carries spectral weight from the f^0 and f^2 configurations; in the Kondo limit the weight of each configuration is approximately Γ_K/D. Since the matrix element on the right-hand side of Eq. (61) projects the f^0 configuration out of the ground state, one would then expect the spectrum of χ_c to comprise a resonance of width proportional to Γ_K at the Fermi level, corresponding to the final-state impurity configuration f^1, and a second resonance, with much smaller spectral weight, at $\epsilon = \Delta$, corresponding to the final-state configuration f^2.

The results in Ref. 70 disagree with these qualitative considerations. A resonance near $\epsilon = \Delta$ (final-state configuration f^2) is found, but its spectral weight, proportional to $1/\Delta$, is much larger than Γ_K. Moreover, there is no Fermi-level resonance, a second peak being instead found near $\epsilon = |\epsilon_f|$ (corresponding to final-state configuration f^0), with weight comparable to that of the f^2 maximum. In contrast with the rounded maxima in Figure 8, the resonances peak at cusps. These are intriguing results, which seem to call for further study of Eq. (61).

C. Tunneling Problem

An outline of the problem of computing the core-hole spectral density for a normal metal has been presented in Section VIII B. In 1970, following the solution of the x-ray absorption problem by Mahan[71] and by Nozières and De Dominicis[72], Ref. 66 obtained the asymptotic expression (59). One year later, Müller-Hartmann et al.[73] calculated the spectral density for an array of N_c core levels. In the single site problem, the final-state core-hole interacts with the conduction electrons. In the N_c-site problem, the core-hole interacts with the conduction states around it and can hop to a neighboring site. The calculation in Ref. 73, on the basis of a bosonization of the model Hamiltonian, concluded that the recoil of the core-hole washes out the infrared divergence of the spectral density and leaves spectral weight at the Fermi level.

Beyond the interest raised by this approximate result, the tunneling of a hole in a metallic environment, pertinent to a variety of physical systems, has received a great deal of attention[74–76]. It has long been recognized that the problem encompasses a competition between energy scales, the characteristic energy being set by the effective tunneling matrix element (or amplitude) t^*[77]. For energies much larger than t^*, the tunneling amplitude can be neglected, and the single-site approximation is adequate. This regime has been extensively studied. For energies comparable to, or much smaller than t^*, by contrast, the problem has been the object of very few studies[73,61].

Recent numerical renormalization-group calculations have shed light on the $N_c = 2$ problem. Apparently distant from the $N_c \rightarrow \infty$ limit, the two-core-levels Hamiltonian nevertheless exhibits the qualitative features separating the multiple-site model from the Doniach-Šunjić model. In special the core-hole potential renormalizes the tunneling matrix element and two fixed points are found: one for energies $\epsilon \gg t^*$, the other for $\epsilon \ll t^*$.

With $N_c = 2$ and the coordinates origin positioned halfway between the sites, the model Hamiltonian conserves parity with respect to exchange of the impurity positions. As in the two-impurity Kondo problem, even (f_{ne}) and odd (f_{no}) Lanczos operators are defined, pro-

jected on which the spinless model Hamiltonian is

$$H_T = \sum_n \epsilon_n^z (f_{n,o}^\dagger f_{n+1,o} + f_{n,e}^\dagger f_{n+1,e} + \text{H. c.})$$
$$-(1/2)(d_e^\dagger d_e - d_o^\dagger d_o)$$
$$+G[(1+S)f_{0e}^\dagger f_{0e} + (1-S)f_{0o}^\dagger f_{0o}](d_e d_e^\dagger + d_o d_o^\dagger)$$
$$-G(1-S^2)(f_{0e}^\dagger f_{0o} + \text{H. c.})(d_e^\dagger d_o + \text{H. c.}), \quad (62)$$

where $S = \sin(k_F R)/k_F R$ (R is the distance between the two sites), and d_e (d_o) annihilates an electron at the even (odd) linear combination of the two core states: d_e (d_o) is the Fermi operator for the bonding (anti-bonding) state constructed out of the core states.

This Hamiltonian has two fixed points[17]: for t = 0, the occupaticns of the site operators $d_1 = (d_e + d_o)/\sqrt{2}$ and $d_2 = (d_e - d_o)/\sqrt{2}$ are conserved. For a single core hole, either $d_1^\dagger d_1 = 0$ and $d_2^\dagger d_2 = 1$ (core hole at site 1) or $d_1^\dagger d_1 = 1$ and $d_2^\dagger d_2 = 0$ (core hole at site 2). Projected on eacli of these two subspaces, the model Hamiltonian is equivalent to that of the single-site model—a single-particle Hamiltonian in which the conduction states are phase shifted by $\delta = \tan^{-1}(-\pi\rho G)$. This fixed point (more precisely a line of fixed points, since each potential G defines a fixed point) is called the atomic-orbital fixed point.

For $t \to \infty$, on the other hand, the second term on the right-hand side of Eq. (62) forces the anti-bonding core orbital to be vacant, so that $d_o^\dagger d_o = 0$ and $d_e^\dagger d_e = 1$. With this, the last term on the right-hand side of Eq. (62) vanishes, which decouples the even conduction band channel from the odd one. Two separate sets of conduction states result: an even one with phase shift δ_e and an odd one with phase shift δ_o. This is referred to as the molecular-orbital fixed point.

Ref.17 has computed the even and the odd spectral densities for the Harniltonian Eq. (62), defined as

$$\rho_p(\epsilon) = \sum_F |\langle F|d_p|\Omega\rangle|^2 \delta(E_F - E_\Omega - \epsilon), \quad (63)$$

with p = e (even) and p = o (odd), respectively.

The results show that, for large ϵ, the two spectral densities coincide, indicating that the scaled Hamiltonian is near the atomic-orbital fixed point—where states of opposite parities are degenerate. At small energies, however, the even and the odd spectral densities are markedly different. Both follow power laws,

$$\rho_p(\epsilon) \sim (\epsilon/D)^{\alpha_p - 1}, \quad (64)$$

but while the exponent for the odd density is the Doniach-Šunjić expression

$$\alpha_o = (\delta_e/\pi)^2 + (\delta_o/\pi)^2, \quad (65)$$

the exponent for the even density has a inodified form

$$\alpha_e = (\delta_e/\pi - 1)^2 + (\delta_o/\pi + 1)^2. \quad (66)$$

To interpret this result, the authors observe that, according to the Friedel sum rule, each term on the right-hand side of the Doniach-Šunjić expression (65) is the square of the cliarge piled up around the impurity in each conduction-band channel[78]. Equation (66) then indicates that one electron has been transferred from the even to the odd channel.

Such a transfer is indeed required by symmetry. In the initial state, both impurity orbitals are occupied. In the final state, at low energies, the hole must be at the anti-bonding (odd) orbital. The initial and final impurity states have therefore opposite parities, and the matrix element $\langle F|d_+|\Omega\rangle$ will therefore vanish unless a cross-channel electron transfer in the conduction band reverses the parity of the final state.

The net result of all this is a divergent odd spectral density [the exponent $\alpha_o - 1$ on the right-hand side of Eq. (64) is always negative] and a vanishing even spectral density (the exponent $\alpha_e - 1$ is positive) at the Fermi level. The $N_i = 2$ spectral density, in contrast with the conclusions of Ref. 73, is singular at the Fermi level; moreover, there is no spectral weight at $\epsilon = 0$.

In the crossover region, the odd density shows no structure, but the even density is strongly peaked at an energy t*, which defines the effective tunneling amplitude. The numerical values obtained for this quantity for a variety of parametrical choices[79] are in excellerit agreement with the exact expression of Yamada et al.[76].

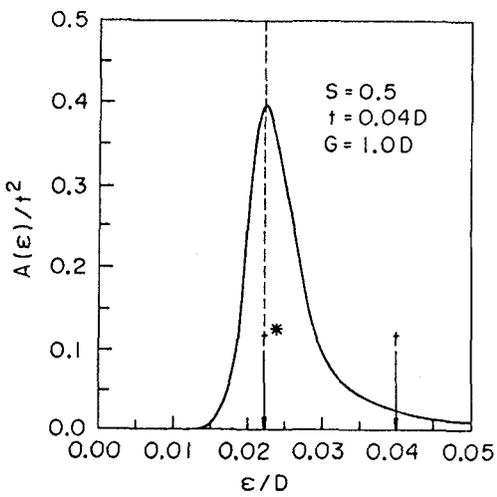

Figure 9.: Tunneling rate for core hole in two-site model. The rate A is given by Eq. (67). The bare tunneling matrix element t and the effective matrix element t* are indicated along the energy axis. The latter is calculated from the analytical expression in Ref. 76. For $\epsilon \gg t^*$, the scaled Hamiltonian is close to the atomic-orbital fixed point, whose properties mimic those of the single-site Hamiltonian. For $\epsilon \ll t^*$, it is close to the molecular-orbital fixed point, in which the impurity antibonding orbital is energetically inaccessible.

A study more faithful to the tunneling problem propounded by Kondo[74] has been carried out by Frota and Mahan[80]. Instead of the spectral density, they have calculated the frequency dependent tunneling rate

$$A(\epsilon) = \sum_F |\langle F|d_1^\dagger d_2|\Omega\rangle|^2 \delta(E_F - E_I - \epsilon), \qquad (67)$$

where $|\Omega\rangle$ is the ground state of the one–core-hole subspace. If G were zero, for positive ϵ the matrix element on the right-hand side would be non-zero only with

$$|F\rangle = d_o^\dagger |\Omega_c\rangle, \qquad (68)$$

where $|\Omega_c\rangle$ is the conduction-band ground state. In this case, the right-hand side of Eq.(67) would consist of a delta function at $\epsilon = t$.

For non-zero core-hole potential, Figure 9 shows that the spike shifts to $\epsilon = t^*$, the effective splitting between the bonding and the anti-bonding levels, and broadens asymmmetrically. On the high-energy side, $\epsilon \gg t^*$, near the atomic-orbital fixed point, the tunneling rate reflects the reaccommodation of the conduction electrons to the sudden change of potential that accompanies the transition of the core hole from one site 1 to site 2, an effect analogous to the infrared divergence of the spectral density in the single-site problem. Since this is the regime accessible to perturbation theory, from various analyses[74,76] $A(\epsilon)$ is expected to grow as a power of (D/ϵ). Figure 9 agrees with such predictions.

For $\epsilon \ll t^*$, close to the molecular-orbital fixed point, the anti-bonding orbital is energetically inaccessible. During the crossover, therefore, the tunneling rate is drastically reduced. The peak energy in Figure 9 coincides with the maximum of the even spectral density calculated in Ref. 17.

IX. Conclusions

The previous sections have examined the physical content of the renormalization-group solutions of various problems, only casual attention being given to other methods. It is now time for a more critical evaluation of the numerical renormalization group procedure, time to compare it with the other approaches, to expose its limitations, and to appraise its potential for future developments.

The theory of localized excitations in metals includes now a number of reliable alternatives to the renormalization-group approach, to which each of them is superior for specific applications. In particular, for the calculation of thermodynamical properties of single-impurity models, the Bethe *ansatz*[9,13] is unrivaled. The $1/N$-expansion methods – the slave-boson approach[81], the non-crossing approximation[82], and the Gunnarsson-Schönhammer variational method[27], among others[10] – have a wider range: they cover thermodynamical and excitation properties. In exchange for the rigor of the Bethe *ansatz*, they offer mathematical simplicity. These methods have demonstrated the low-energy photoemission peaks observed in such valence-fluctuation compounds as $CeAl_3$ to be Kondo resonances, which has explained a long-standing puzzle in the theory of the rare earths[27]. They nevertheless have limitations: plain spin-degeneracy is outside their reach, and in spite of earnest attempts to analyze multiple-impurity or periodic systems, the results they have yielded are far less satisfactory than the solutions of the single-particle models[83].

The quantum Monte-Carlo method[12,67,84] is able to calculate thermodynamical and dynamical properties and to deal with multiple impurities and lattice systems. Nonetheless, it is somewhat limited by the "sign problem"', which has only been satisfactorily circumvented for particle-hole symmetric problems. Also, although it can reach relatively low temperatures (e. g., temperatures an order of magnitude smaller than the Kondo temperature for typical choices of the Anderson-model parameters), its inability to probe the ground state is in certain cases a serious shortcoming—one that can perhaps explain the failure of the method to find a divergent susceptibility at the unstable-fixed-point two-impurity Kondo Hamiltonian[58].

Still unknown are the limitations of the most recently developed method, that of conformal mapping[11]. Problems analysed so far have been restricted to the vicinity of fixed points, but extensions are likely to appear. Apart from being elegant and able to calculate thermodynamical and dynamical properties, that technique is attractive because it has fundamental concepts and structures—e. g., fixed points, relevant, operators—in common with renormalization-group theory. As a consequence, tandem calculations, the numerical procedure checking hypothesis of the analytical one, the latter checking the accuracy of the former have proved fruitful[53].

This consorting of two procedures finds parallels in the relationship between the renormalization group and the other methods in the theory of strongly correlated systems. The numerical renormalization group method has contributed decisively to the solution of a list of problems headed by the calculation of the physical properties for the Anderson Hamiltonian[85]. In each case, the procedure described in Section IV has unraveled the physics of a model and established bench marks—which later provided checks on the accuracy of other numerical methods and served to support assumptions in analytical methods. In this, three characteristics of the renormalization-group calculations have been essential: (i) the theory of the renormalization group identifies fixed points and allows perturbative expansions in their vicinity; with them, large fractions of the temperature or energy axes can be scanned analytically, although numerical analysis is needed to treat the crossovers; (ii) the approximations involved in the nu-

merical procedure are fully controllable, the discretization of the conduction band controlled by the parameter **A** and the infrared and ultraviolet truncations needed in the numerical diagonalization controlled by the number of states kept; (iii) the procedure is uniformly accurate over the parametrical space of the model, so that the deviations in the calculation of a given property at a given energy or temperature can be estimated from analytical computations for trivial choices of the model parameters.

Given these assets, one can imagine that the technique here surveyed will continue to do groundwork for other methods. The central obstacle facing applications has been the exponential growth of the computational cost with the number of electronic degrees of freedom. This difficulty is less severe than it used to be, since Ref. 86 has shown that the generalized procedure in Section IV allows accurate calculations with **A** as large as 10; with existing computer resources reliable computations of thermodynamical as well as dynamical properties for two-impurity models are now feasible. Broader generalizations are nonetheless needed to extend the method to larger cliisters and, most importantly, to periodic systems. Generalizations with these purposes are currently under study.

Acknowledgments

This work has been continuously supported by the Fundaçiio de Amparo à Pesquisa de São Paulo (FAPESP), the Conselho Nacional de Desenvolvimento Científico e Tecnológico (CNPq), the Coordenação de Aperfeiçoamento de Pessoal de Nível Superior (CAPES), and the Financiadora Nacional de Estudos e Projetos (FINEP).

References

1. J. Kondo, in Solid State Physzcs, H. Ehrenreich, F. Seit::, and D. Turnbull, eds. (Academic, New York, 1969) vol. 23, p. 183.
2. D. M. Newns, Phys. Rev. 178, 1123 (1969).
3. See var ous articles in Valence *Instabilities* and *Related* Narrow Band Phenomena, ed. R. D. Parks (Plenurn, New York, 1977).
4. G. R. Stewart, Rev. Mod. Phys. 56, 755 (1985).
5. P. W. Anderson and G. Yuval, Phys. Rev. Lett. 28, 89 (1969); Phys. Rev. B **1,** 1522 (1970).
6. K. G. Wilson, Rev. Mod. Phys. 47, 773 (1975).
7. H. R. Krishna-murthy, K. G. Wilson, and J. W. Wilkins, Phys. Rev. Lett. 35, 1101 (1975); H. R. Krishna-murthy, J. W. Wilkins, and K. G. Wilson, Phys. Rev. B 21, 1003 (1980).
8. J. R. Schrieffer and P. A. Wolff, Phys. Rev. 149, 491 (1936).
9. P. Schlottman, Phys. Rep. **181,** 1 (1989).
10. N. E. Bickers, Rev. Mod. Phys. 59, 845 (1987).
11. I. Affleck, Nucl. Phys. B 352, 849 (1990); I. Affleck and A. W. W. Ludwig, Nucl. Phys. B 360, 641 (1991); Phys. Rev. Lett. 67, 161 (1991).
12. J. E. Hirsch and R. M. Fye, Phys. Rev. Lett. 56, 2521 (1986); R. M. Fye, J. E. Hirsch, and D. J. Scalapino, Phys. Rev. B 35, 4901 (1987).
13. A. M. Tsvelick and P. B. Wiegmann, Adv. Phys. 32, 453 (1983); N. Andrei, K. Furuya, and J. H. Lowenstein, Rev. Mod. Phys. 55, 331 (1983).
14. B. A. Jones and C. M. Varma, Phys. Rev. Lett. 58, 843 (1987).
15. B. A. Jones, C. M. Varma, and J. W. Wilkins, Phys. Rev. Lett. 61, 125 (1988).
16. B. A. Jones and C. M. Varma, Phys. Rev. B 40, 324 (1989).
17. V. L. Líbero and L. N. Oliveira, Phys. Rev. Lett. 65, 2042 (1990).
18. H. O. Frota and L. N. Oliveira, Phys. Rev. B 33, 7871 (1986).
19. C. M. Varma, Rev. Mod. Phys. 48, 219 (1976).
20. M. Campagna, E. Bucher, G. K. Wertheim, L. D. Longinetti, Phys. Rev. Lett. 33, 165 (1974).
21. J. M. D. Coey, S. K. Ghatek, and F. Holtzberg, AIP Conf. Proc. 24, 38 (1974), quoted in Ref. [19].
22. N. W. Ashcroft and N. D. Mermin, *Solid State* Physics (Holt, Rinehart and Winston, New York, 1976).
23. B. Maple and D. Wohleben, Phys. Rev. Lett. 27, 511 (1971).
24. P. W. Anderson, Phys. Rev. 124, 41 (1961).
25. H. R. Krishna-murthy, J. W. Wilkins, and K. G. Wilson, Phys. Rev. B 21, 1044 (1980).
26. J. W. Wilkins, in Valence Instabilities, P. Watcher and H. Boppart, eds. (North-Holland, Amsterdam, 1982), p. 1.
27. O. Gunnarsson and K. Schonhammer, Phys. Rev. Lett. 50, 604 (1983); Phys. Rev. B 28, 4315 (1983); 28, 7330 (1983).
28. P. A. Lee, T. M. Rice, J. W. Serene, L. J. Sham, and J. W. Wilkins, Commun. Solid State Phys. 12, 99 (1986).
29. The Sm ions in SmS and other ions in valence-fluctuation compounds are not impurities, either. They, too, develop coherent behavior at sufficiently low temperatures. Nevertheless, the unusual very-low–temperature properties of the heavy-fermion materials constitute a more colorful example.
30. A renormalization-group analysis of the emergente of coherence in heavy-fermion systems has been carried out by M. A. Continentino, G. M. Japiassu, and A. Troper, Phys. Rev. B 39, 9734 (1989).
31. M. Yoshida, M. A. Whitaker, L. N. Oliveira, Phys. Rev. B 41, 9403 (1990).
32. See, e. g., R. Haydock, in *Solid State* Physzcs, *H.*

Ehrenreicli, F. Seitz, and D. Turnbull, eds. (Academic, New York, 1980) vol. 35, p. 215.
33. A. Abrikosov, Physics 2, 5 (1965).
34. H. Suhl, Physics 2, 39 (1965); Phys. Rev. **141**, 483 (1966).
35. Y. Nagaoka Phys. Rev. **138A**, 1112 (1965).
36. G. Toulouse, C. R. Acad. Sci. 268, 1200 (1969).
37. L. N. Oliveira and J. W. Wilkins, Phys: Rev. Lett. 47, 1553 (1981).
38. K. Yosida and K. Yamada, Prog. Theor. Phys. 53, 1286 (1975); K. Yamada, Prog. Theor. Phys. 54, 316 (1975).
39. P. Nozières, J. Low. Temp. Phys. 17, 31 (1974); Proceedings of the 14th *International Conference* on Low *Temperature* Physics, M. Kursius and M. Vuorio, eds. (North-Holland, Amsterdam, 1975), vol. 5, p. 339.
40. F. D. Haldane, Phys. Rev. Lett. 40, 416 (1978); 911 (E) (1978).
41. R. Allub, H. Ceva, and B. R. Alascio, Phys. Rev. B 29, 3098 (1984).
42. J. Mazaferro, C. A. Balseiro, and B. Alascio, Phys. Rev. B 47, 274 (1981).
43. H. Bjerrum Møller, S. M. Shapiro, and R. J. Birgeneau, Phys. Rev. Lett. 39, 1021 (1977).
44. Y. Yafet, C. M. Varma, and B. A. Jones, Phys. Rev. B 32, 360 (1985).
45. N. Read, K. Dharmvir, J. W. Rasul, and D. M. Newns, J. Phys. C 19, 1597 (1986); for a similar aiialysis for uranium ions, see A. C. Nunes, J. W. Rasul, and G. A. Gehring, J. Phys. C 19, 1017 (1986).
46. Y. Shimizu, O. Sakai, and T. Kasuya, Physica B 163, 401 (1990).
47. M. Baliña and A. A. Aligia, Physica B 171, 109 (1991).
48. B. Alascio, R. Allub, and C. A. Balseiro, Phys. Rev. B 34, 4786 (1986).
49. H. O. Frota and G. D. Mahan, Phys. Rev. B 43, 10755 (1991).
50. D. M. Cragg and P. Lloyd, J. Phys. C **11**, L597 (1978); 12, L215 (1979); D. M. Cragg, P. Lloyd, and P. Nozières, J. Phys. C 13, 803 (1980).
51. P. Nozières and A. Blandin, J. Phys (Paris) 41, 193 (1980).
52. D. L. Cox, Phys. Rev. Lett. 59, 1240 (1987).
53. I. Affleck, A. W. W. Ludwig, H.-B. Pang, and D. L. Cox, Phys. Rev. B 45, 7918 (1992).
54. K. Flensberg and H. O. Frota, Solid State Commun. 77, 917 (1991).
55. S. Hershfield, J. H. Davies, and J. W. Wilkins, Phys. Rev. Lett. 67, 3720 (1991).
56. S. Alexander and P. W. Anderson, Phys. Rev. 133, A1594 (1964).
57. C. Jayaprakasli, H. R. Krishnamurthy, and J. W. Wilkins, Phys. Rev. Lett. 47, 737 (1981).
58. R. M. Fye and J. E. Hirsch, Phys. Rev. B 40, 4780 (1989).
59. I. Affleck and A. W. W. Ludwig, Phys. Rev. Lett. 68, 1046 (1992).
60. L. N. Oliveira and J. W. Wilkins, Phys. Rev. B 24, 4863 (1981); Phys. Rev. B 32, 696 (1985); D. L. Cox, H. O. Frota, L. N. Oliveira, and J. W. Wilkins, Phys. Rev. B 32, 555 (1985); M. A. Whitaker and L. N. Oliveira, Physica B 171, 69 (1991).
61. D. E. Heim, Phys. Rev. B 33, 5254 (1986).
62. O. Sakai, Y. Shimizu, and T. Kasuya, J. Phys. Soc. Jpn. 58, 3666 (1989); Solid State Comm. **75**, 82 (1990); 0 . Sakai, Y. Shimizu, R. Takayama, and T. Kasuya, Physica B 163, 695 (1990).
63. The discretization of the conduction band renormalizes the model parameters G and Γ to G/A_Λ and Γ/A_Λ, respectively, Eq. (34) defining A_Λ. To counteract this reduction, prior to each numerical computation, G and Γ are multiplied by A_Λ.
64. L. N. Oliveira, V. L. Líbero, H. O. Frota, and M. Yoshida, Physica B 171, 61 (1991).
65. D. C. Langreth, Phys. Rev. 150, 516 (1966).
66. S. Doniach and M. Šunjić, J. Phys. C 3, 284 (1970).
67. R. N. Silver, J. E. Gubernatis, D. S. Sivia, and M. Jarrel, Phys. Rev. Lett. 65, 496 (1990).
68. H. O. Frota, Phys. Rev. B 45, 1096 (1992).
69. J. J. S. Brito and H. O. Frota, Phys. Rev. B 42, 6378 (1990).
70. H. O. Frota, Phys. Rev. B 44, 8433 (1991).
71. G. D. Mahan, Phys. Rev. 163, 612 (1967); in Solid State Physics, H. Ehrenreich, F. Seitz, and D. Turnbull, eds. (Academic, New York, 1974) vol. 29, p. 75.
72. P. Nozières and C. T. De Dominicis, Phys. Rev. B 178, 1097 (1969).
73. E. Müller-Hartmann, T. V. Ramakrishnan, and G. Toulouse, Phys. Rev. B 3, 1102 (1971).
74. J. Kondo, Physica B 84, 40 (1976).
75. K. Vladar, A. Zawadowski, and G. T. Zimányi, Phys. Rev. B 37, 2001 (1988); Phys. Rev. B 37, 2015 (1988); Y. Kagan and N. Y. Prokof'ev, JETP 63, 1276 (1986).
76. K. Yamada, A. Sakurai, and M. Tokashige, Prog. Theor. Phys. 70, 73 (1983); K. Yamada, A. Sakurai, M. Miyazima, and H. S. Hwang, Prog. Theor. Phys. 75, 1030 (1986).
77. The effective matrix element t^* is smaller than the bare tunneling matrix element t, because the hole must carry the conduction-band charge piled around it as it hops from site to site.
78. K. Schotte and U. Schotte, Phys. Rev. 185, 479 (1969); Phys. Rev. 185, 509 (1969).
79. V. L. Líbero and L. N. Oliveira, Physica B 171, 106 (1991).
80. H. O. Frota and G. D. Mahan, to appear in Phys. Rev. B.

81. **A.** C. Hewson, D. M. Newns, J. W. Rasul, **H.-U.** Desgranges, and P. Strange, in Theoy of Heavy *Fermions* and *Valence* Fluctuations, T. Kasuya and T. Saso, eds. (Springer, Berlin, 1985), p. 134.
82. N. E. Bickers, D. L. Cox, and J. W. Wilkins, Phys. Rev. Lett. 54, 230 (1985); Phys. Rev. B 36, 2036 (1987).
83. For a discussion of this point in the context of the twa-impurity Kondo model, see B. **A.** Jones, Physica B 171, **53** (1991).
84. M. E. Jarrel, J. E. Gubernatis, and R. N. Silver, Phys. Rev. B 44, 5347 (1991).
85. The other problems on the list are those analysed in Refs. 7, 14, 17. The computation of the spectral density for the Anderson model was preceded by the $1/N$-expansion solution (Ref.27).
86. V. L. Líbero and L. N. Oliveira, Phys. Rev. B 42, 3167 (1990).